The Astrophysical Journal, 1002:208 (24pp), 2026 May 10 https://doi.org/10.3847/1538-4357/ae5620

# A New Look into the Atmospheric Composition of WASP-39 b

Sushuang Ma[1], Arianna Saba[1], Ahmed Faris Al-Refaie[2], Giovanna Tinetti[1], Sergei N. Yurchenko[2], Jonathan Tennyson[2], and Cesare Cecchi-Pestellini[3]

[1] Department of Physics, Faculty of Natural, Mathematical & Engineering Sciences, King's College London, Strand, WC2R 2LS London, UK
[2] Department of Physics and Astronomy, University College London, Gower Street, WC1E 6BT London, UK
[3] INAF—Osservatorio Astronomico di Palermo, P.za Parlamento 1, 90134 Palermo, Italy

*Received 2025 April 10; revised 2026 March 10; accepted 2026 March 19; published 2026 May 7*

## Abstract

Being one of the first exoplanets observed by the James Webb Space Telescope, WASP-39 b has become an iconic target, and many transit spectra recorded with different instruments (NIRISS, NIRCAM, NIRSpec G395H, NIRSpec PRISM, and MIRI) are currently available, allowing in-depth studies of its atmosphere. We present here a novel approach to interpret WASP-39 b's transit spectroscopic data, consisting of a multistep process where ab initio equilibrium chemistry models and blind retrievals are used iteratively to find physically robust, optimal solutions. Following this approach, we have identified a new scenario to explain WASP-39 b's atmospheric composition, in which silicon-based chemistry plays a major role. In this scenario, SiO may explain the spectral absorption at 4.1 $\mu$m, currently interpreted as being due to $SO_2$. SiO and the other gas species identified by the retrieval models, i.e., $H_2O$, $CO_2$, Na, and K, are consistent with an atmosphere in chemical equilibrium with a temperature–pressure profile constrained by $H_2O$ and $CO_2$ absorption bands. In addition, silicate clouds and hazes can produce the spectral features observed by MIRI in the spectral window 5–12 $\mu$m. While we advocate the need for more data, possibly at higher spectral resolution, to confirm our results for WASP-39 b's atmospheric composition, we highlight a refined atmospheric retrieval strategy with preselection and post-reconstruction to guide the next generation of transit spectroscopy.

*Unified Astronomy Thesaurus concepts:* Exoplanet atmospheres (487); Exoplanet astronomy (486); Transmission spectroscopy (2133)

## 1. Introduction

### 1.1. First WASP-39 b Observations

WASP-39 b has been among the first exoplanets observed by the James Webb Space Telescope (JWST) shortly after its commissioning phase in 2022 (J. Rigby et al. 2023). The planet was discovered by the ground-based transit survey SuperWASP (F. Faedi et al. 2011). Their analysis indicated WASP-39 b to be a highly inflated Saturn-like exoplanet, with a mass of 0.28 ± 0.03 $M_J$ and a radius of 1.27 ± 0.04 $R_J$. The study also estimated an equilibrium temperature of ∼1100 K. The parent star, WASP-39 A, was studied by F. Faedi et al. (2011), L. Mancini et al. (2018), A. S. Bonomo et al. (2017), and G. Maciejewski et al. (2016), among others; it is a G8 type star with a mass of 0.93 ± 0.03 $M_\odot$, a radius of 0.895 ± 0.023 $R_\odot$, an effective temperature of 5400 ± 150 K and [Fe/H] of −0.12 ± 0.1. The stellar age was estimated to be 8.5–9 Gyr (A. S. Bonomo et al. 2017; L. Mancini et al. 2018).

Prior to JWST, observations of WASP-39 b using the Wide Field Camera 3 (WFC3) onboard the Hubble Space Telescope (HST) indicated the presence of water vapor in its atmosphere (C. Fisher & K. Heng 2018; A. Pinhas et al. 2018, 2019; A. Tsiaras et al. 2018; H. R. Wakeford et al. 2018). Additionally, sodium and potassium were suggested by observations using HST's Space Telescope Imaging Spectrograph (STIS; P. D. Fischer et al. 2016; D. K. Sing et al. 2016), the ground-based VLT (0.411–0.810 $\mu$m; N. Nikolov et al. 2016), and the LRG-BEASTS survey (0.4–0.9 $\mu$m; J. Kirk et al. 2019). H. R. Wakeford et al. (2018) and J. Kirk et al. (2019) reported highly supersolar metallicities to interpret these datasets. D. Thorngren & J. J. Fortney (2019) estimated the maximum atmospheric metallicity of WASP-39 b to be 54.5× solar.

A. Saba et al. (2025) analyzed archive data obtained with the STIS and WFC3 instruments of WASP-39 at various epochs. The metrics used as stellar activity indicators leaned toward WASP-39 being an inactive star. These results are in agreement with previous studies (D. K. Sing et al. 2016; L. Mancini et al. 2018), with the exception of A. Pinhas et al. (2018), who suggested stellar heterogeneities.

### 1.2. JWST Observations of WASP-39 b

Transit spectra of WASP-39 b using different JWST's instrument modes were published by E.-M. Ahrer et al. (2023; NIRCam, 2.4–4.0 $\mu$m), A. D. Feinstein et al. (2023, NIRISS, 0.6–2.8 $\mu$m), L. Alderson et al. (2023; NIRSpec G395H, 2.7–5.2 $\mu$m), Z. Rustamkulov et al. (2023; NIRSpec PRISM, 0.5–5.5 $\mu$m), and S. Sarkar et al. (2024; NIRSpec G395H & PRISM). A single transit of WASP-39 b was observed by NIRISS in SOSS mode on 2022 July 26; by NIRCAM in both long-wavelength (LW) and short-wavelength (SW) channels on 2022 July 22–23; by NIRSpec with its G395H grating using the Bright Object Time Series mode (BOTS) on 2022 July 30–31 and in the PRISM mode on 2022 July 10. Additionally, it was observed with MIRI low-resolution spectroscopy (LRS), from 5 to 12 $\mu$m, on 2023 February 14. By combining all available JWST observations of WASP-39 b, we obtain a spectral coverage from 0.6 to 12 $\mu$m.

The transit data obtained with each of these instruments have undergone extensive scrutiny by the exoplanet community (E. Esparza-Borges et al. 2023; D. Grant et al. 2023; JWST Transiting Exoplanet Community Early Release Science Team et al. 2023; A. J. Louca et al. 2023; S.-M. Tsai et al. 2023a, 2023b; A. Arfaux & P. Lavvas 2024; N. Khorshid et al. 2024; J. Roy-Perez et al. 2025). A variety of data analysis pipelines, saturation handling techniques (S. Sarkar et al. 2024), noise mitigation methods (M. Holmberg & N. Madhusudhan 2023), and spectral extraction algorithms (A. Darveau-Bernier et al. 2022) have been developed. Beyond providing open access to the data, one of the goals of the ERS program was to invite the community to perform independent data analysis and compare results. NIRISS data were reduced with six different pipelines: `nirHiss` (T. Bell et al. 2022; A. D. Feinstein et al. 2023), `exoTEDRF` ( M. Radica et al. 2023; M. Radica 2024), `Transitspectroscopy` (N. Espinoza 2022), `Iraclis` (A. Tsiaras et al. 2016), `NAMELESS`, `FIREFLy` (Z. Rustamkulov et al. 2022). NIRCAM data were processed using `Eureka!` (T. Bell et al. 2022), `tshirt`, `HANSOLO` (M. Lendl et al. 2016, 2017) and `chromatic-fitting`. NIRSpec G395H data were reduced by six separate teams using `ExoTiC-JEDI` (L. Alderson et al. 2022), `Aesop`, ExoTEP (B. Benneke et al. 2019), `Tiberius` (J. Kirk et al. 2019), and `Transitspectroscopy`. For NIRSpec PRISM data, `Eureka!`, `Tiberius`, `FIREFLy`, and `tshirt` were utilized. MIRI LRS data were processed with `Eureka!`, `Tiberius`, and `SPARTA` (E. M. R. Kempton et al. 2023).

The data obtained with different JWST instrument modes have not always suggested a consistent story, possibly due to uncertainties in instrumental performance and/or reduction processes (e.g., M. Holmberg & N. Madhusudhan 2023; J. J. Davey et al. 2024; A. Lueber et al. 2024). For instance, depending on the instrument mode used, WASP-39 b's C/O ratio has been reported to be substellar (E.-M. Ahrer et al. 2023), subsolar (A. D. Feinstein et al. 2023), subsolar to solar (L. Alderson et al. 2023), or supersolar (Z. Rustamkulov et al. 2023). It is known that different data pipelines can potentially produce inconsistent results (L. V. Mugnai et al. 2024): this inconsistency can pose challenges when combining datasets processed by different pipelines. Offsets in the spectral data may arise due to different data analysis approaches, variations in intrinsic instrumental calibrations, and different choices of system parameters (see, e.g., K. H. Yip et al. 2021). Currently, no single pipeline has been used to uniformly reduce WASP-39 b's data from all JWST instruments and their corresponding observing modes. We use here the spectral data published in A. L. Carter et al. (2024) and D. Powell et al. (2024) for the reasons described below.

Although the datasets for WASP-39 b were processed using different data reduction pipelines, A. L. Carter et al. (2024) selected the nominal reductions for each available dataset. They used `Eureka!` to extract a white light curve from each JWST dataset, resulting in a total of seven light curves: NIRISS order 1 and order 2, NIRSpec G395H NRS 1 and NRS 2, NIRSpec PRISM, NIRCam SW photometric channel, and LW spectroscopic channel. A joint white light-curve fitting with `juliet` (N. Espinoza et al. 2019) was performed, incorporating one TESS light curve, six NGTS light curves, and radial velocity measurements from CORALIE and SOPHIE. This combined fitting yielded highly precise constraints on the system parameters, achieving a minimum precision of 0.5%. `Eureka!` was also used to extract chromatic light curves at native resolution for each JWST dataset. The spectral light-curve fitting was performed by fixing the orbital parameters to those derived from the joint fitting. This procedure ensured a reduction in the observable offsets among the initial data release presented in A. Lueber et al. (2024). A. L. Carter et al. (2024) applied an additional manual offset of −177 ppm to the NIRSpec PRISM data. Moreover, their final combined spectrum excluded the saturated region of the NIRSpec PRISM data between 0.62–2.1 $\mu$m.

MIRI observations were scheduled approximately seven months after the observations were recorded with NIRISS, NIRSpec, and NIRCam. MIRI transit data were observed in the LRS slitless prism mode at an average resolution of approximately 100. D. Powell et al. (2024) report that the white light-curve fitting of MIRI data performed with `Eureka!` adopted the same orbital parameters as those used by A. L. Carter et al. (2024). Although the MIRI data were reduced with three different pipelines, we include here only the reduction obtained with `Eureka!` to minimize offsets. This choice ensures further consistency across all instruments. Meanwhile, L. Flagg et al. (2024) have suggested that MIRI data beyond 10 $\mu$m might be contaminated by circumstellar debris disk features that need to be considered in data analysis.

### 1.3. Scientific Interpretation of WASP-39 b Transit Spectra Recorded with JWST

Various molecules were reported in the literature to be present in the atmosphere of WASP-39 b, including $H_2O$, CO, $CO_2$, K, $H_2S$, and $CH_4$ (E.-M. Ahrer et al. 2023; L. Alderson et al. 2023; E. Esparza-Borges et al. 2023; A. D. Feinstein et al. 2023; Z. Rustamkulov et al. 2023; A. Lueber et al. 2024; S. Constantinou & N. Madhusudhan 2024). There are also tentative detections of $SO_2$ from S.-M. Tsai et al. (2023a), L. Alderson et al. (2023), Z. Rustamkulov et al. (2023), S. Constantinou & N. Madhusudhan (2024), and D. Powell et al. (2024). A. Lueber et al. (2024) reexamined the spectral feature around 4.1 $\mu$m attributed to $SO_2$ absorption and suggested that its interpretation appears to be model-dependent; models with clouds favor the detection of $SO_2$ in the NIRSpec PRISM spectrum. They also discussed the use of gray clouds and nongray ones, as implemented in `BeAR` (D. Kitzmann et al. 2020), in the simulations.

A. Lueber et al. (2024) considered $CH_4$, $H_2O$, CO, $CO_2$, and $SO_2$ as C- and O-bearing molecules in their retrieval simulations of NIRCAM and NIRSpec PRISM ERS spectra. Their retrieved values of C/O using random forest are consistent with the stellar value of 0.46 ± 0.09 from A. S. Polanski et al. (2022). Their NIRSpec PRISM free retrieval results are closer to the solar value of 0.55 from M. Asplund et al. (2009; see Figure 13 in A. Lueber et al. 2024). Their nested-sampling retrievals suggest C/H and O/H values to be consistent with solar.

The spread in the reported metallicities in the literature suggests that factors beyond instrumental modes may play a role in these discrepancies. For instance, when using different data analysis techniques, L. Alderson et al. (2023), A. D. Feinstein et al. (2023), and Z. Rustamkulov et al. (2023) reported supersolar metallicities, E.-M. Ahrer et al. (2023) constrained it to be solar to supersolar, while A. Lueber et al. (2024) found subsolar to solar metallicity in most of the free retrievals and supersolar metallicity in the random-forest retrieval. Another identified source of discrepancy is the spectroscopic line lists used to interpret the data. For example, P. Niraula et al. (2023) tested different opacity sources and found different abundances of the same molecules.

### *1.4. Retrieval Techniques*

Spectral retrieval methods have often been used in recent years to interpret exoplanetary atmospheric spectra. These algorithms use statistical techniques and high-performance computers to sample a broad parameter space and to search for optimized solutions through a considerable number of iterations. Robust convergence, especially in high-dimensional retrievals, requires a large number of iterations and steps, making the computing power requirements more onerous. A notable example of such sampling algorithms is Multinest (F. Feroz & M. P. Hobson 2008; F. Feroz et al. 2019, 2009), a Bayesian inference tool that calculates the evidence with an associated error estimate while generating posterior samples from distributions that may exhibit multiple modes and complex degeneracies in high dimensions.

Constraining the atmospheric temperature–pressure (*T–p*) profile in the case of exoplanets has been a challenge prior to the launch of JWST (see, e.g., V. Bourrier et al. 2020; D. Kitzmann et al. 2020; Q. Changeat et al. 2022; A. Novais et al. 2025). These studies indicated that the quality of the observations was not good enough to constrain *T–p* profiles in retrievals. By contrast, M. Rocchetto et al. (2016) and S. Schleich et al. (2024) have demonstrated the necessity of considering nonisothermal retrievals to interpret transit spectra correctly, especially when thermal inversions are present. Q. Changeat et al. (2025) performed retrievals using the *N*-point profiles on both Titan occultation data from Cassini and JWST and HST transit data of hot Jupiters, including WASP-39 b. Three-dimensional effects, particularly the inhomogeneity of *T–p* profiles across the limbs and poles, are likely to have an impact as well in the retrieval of vertical thermal profiles (C. Fisher et al. 2024; Z. Chen et al. 2025; J. W. Skinner & S. Wei 2025; S. Tada et al. 2025). However, it is not easy to isolate these effects from other contributions. Phase-curve observations are, in principle, more informative to constrain said inhomogeneities.

Our paper focuses on improving the atmospheric retrieval strategy, using WASP-39 b as an example. Our approach has led to a different interpretation of the available JWST data, opening up a new perspective in our understanding of the chemical composition of WASP-39 b and other similar planets.

## 2. Methodology

### *2.1. Possible Offsets among Spectra Recorded with Different Instruments*

We used the observational data described in Section 1.2 and detailed in Table 1. For our retrieval experiments, we used a resolution of ∼100 for each instrument to maintain a uniform resolution across instruments and modes. However, we have tested our results at higher spectral resolution in the spectral ranges where higher resolution data are available. We followed A. L. Carter et al. (2024) and applied a manual offset of –177 ppm to the NIRSpec PRISM data, while adding 68 ppm offset to the NIRISS (we assumed orders 1 and 2 have the same offsets) data and 132 ppm to NIRCam according to the NIRSpec data. To align with the shorter wavelengths, we add a 420 ppm offset to MIRI data. The final data we use in further atmospheric analysis is shown in Figure 1

**Table 1**
Datasets and Reduction Algorithms Used in This Study with Native Spectral Resolution and Offsets Applied

| Instrument Mode | Reduction Algorithms | Native Res. | Offset (ppm) |
|---|---|---|---|
| NIRISS SOSS | `exoTEDRF` | 350–1390 | 68 |
| NIRSpec G395H | `ExoTiC-JEDI` | 1340–2630 | 0 |
| NIRSpec PRISM | `FIREFLy` | 20–290 | −177 |
| NIRCam LW | `Eureka!` | 850–1360 | 132 |
| MIRI LRS | `Eureka!` | 100 | 420 |

### *2.2. Transit and Atmospheric Models*

#### *2.2.1. TauREx*

`TauREx 3` (A. F. Al-Refaie et al. 2021, 2022) is a state-of-the-art modeling framework to simulate exoplanetary atmospheres and to interpret exoplanet atmospheric data collected with different techniques through inverse models based on Bayesian statistics. Several plugins can be activated to simulate, e.g., atmospheric chemistry (A. F. Al-Refaie et al. 2022), cloud microphysics (S. Ma et al. 2023), stellar activity (A. Thompson et al. 2024), and phase-curve interpretation (Q. Changeat et al. 2024). Parameters that are included and tested in retrievals with `TauREx 3` include, but are not limited to, instrumental, atmospheric thermal, chemical, and cloud profiles, as well as planetary and stellar parameters. The radiative transfer calculations performed by `TauREx 3` include molecular/atomic/ionic opacities, Rayleigh and Mie scattering, and collision-induced absorptions (CIAs).

#### *2.2.2. GGChem*

`GGChem` (P. Woitke et al. 2018) is an equilibrium chemistry model that estimates the chemical abundances by minimizing the system's Gibbs' Free Energy, including scenarios with equilibrium condensation and charged particles. The elemental abundances adopted as initial conditions can be customized. A comparison and cross validation of all the chemical equilibrium models implemented in `TauREx 3` can be found in A. F. Al-Refaie et al. (2022). These include `GGChem`, `FastChem` (J. W. Stock et al. 2018), and `ACE` (M. Agúndez et al. 2020, 2012).

#### *2.2.3. YunMa*

`YunMa` (S. Ma et al. 2023) includes cloud microphysics models to estimate the vertical size distributions of cloud particles expected in an atmosphere according to its thermodynamical and chemical conditions, following, e.g., the approach described in A. S. Ackerman & M. S. Marley (2001; A–M hereafter). `YunMa` can also adopt simplified assumptions, such as homogeneous particle size (HPS) distributions, when there is limited knowledge of the atmospheric conditions and/or efficiency needed for retrieval studies. The current `YunMa` estimates cloud opacities using the Bohren–Huffman–Mie approach (C. F. Bohren & D. R. Huffman 2008) of the cloud particles' Mie scattering and absorption, from refractive indices available in the

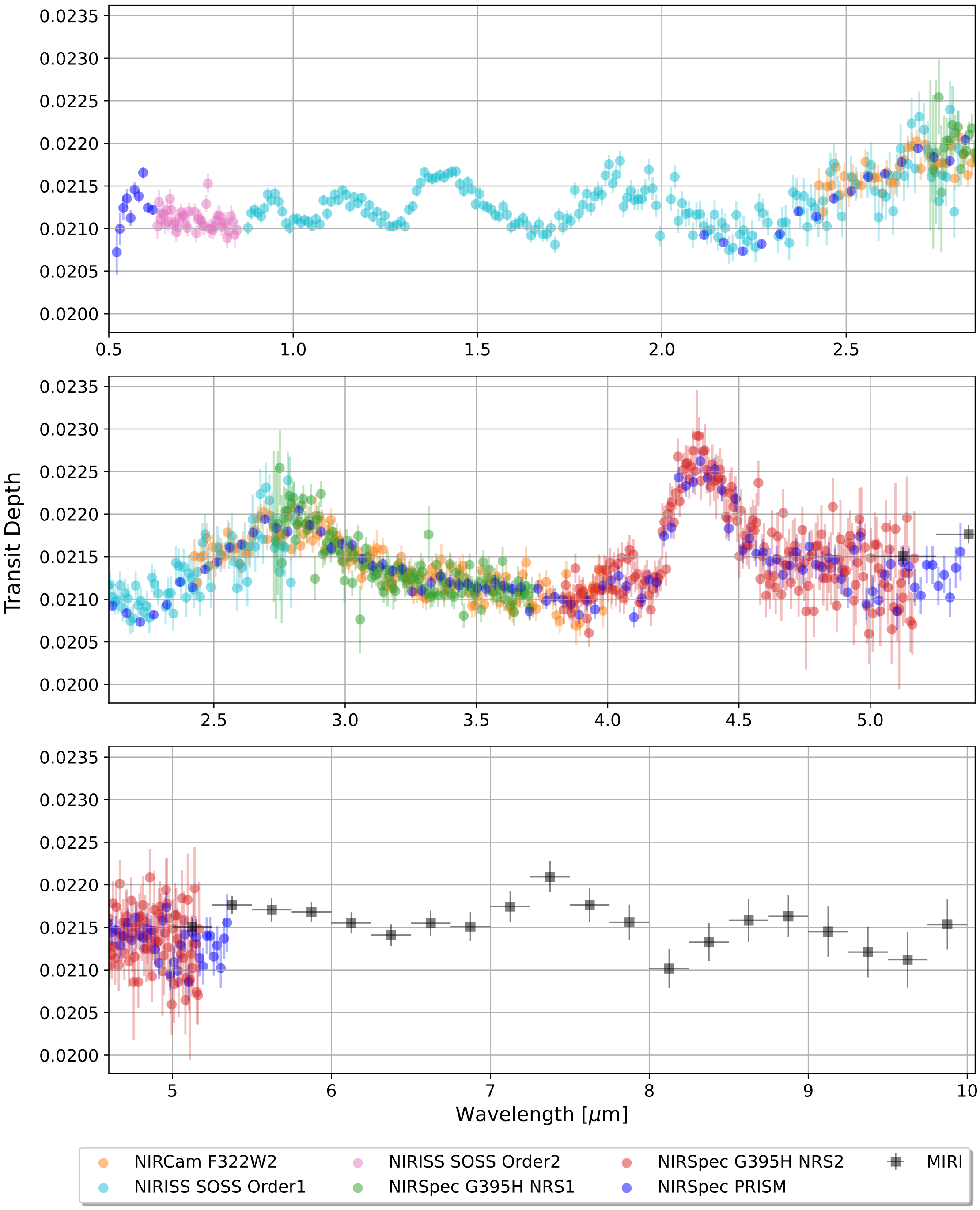

**Figure 1.** JWST NIRISS, NIRCam, NIRSpec, and MIRI observations of WASP-39 b with offsets. The original NIRISS, NIRCam, and NIRSpec data are from A. L. Carter et al. (2024), and the MIRI data are from D. Powell et al. (2024). We tuned the offsets according to data in resolutions available; from resolving power of 100 to native resolutions, and here we plotted the native resolution of NIRSpec PRISM data, and one-fifth native resolution for the rest of the instruments and modes. We added offsets to data from each instrument using the NIRSpec data as a baseline, as detailed in the main text.

literature. When integrated into `TauREx 3`, `YunMa` enables the generation of, or retrieval from, transmission and emission spectra of cloudy atmospheres.

### *2.3. Hybrid Approach Adopted Here*

To interpret the JWST's observations of WASP-39 b, we adopt here a novel approach that combines free retrievals and ab initio models to explore more efficiently the parameter space of possible, physically viable solutions compatible with the data, as depicted in Figure 2. We first use equilibrium chemistry models, assuming certain metallicity values, elemental ratios, and thermodynamic conditions, to estimate the most plausible gaseous and condensed species—*Eq.*—expected to be present in the atmosphere (Step 1). Then, we perform a spectral retrieval analysis (with `TauREx 3` and `YunMa`) with a subsample of the chemical species identified in Step 1 as priors, selecting those that have a detectable spectral signature in the wavelength range probed by the observations. We then compare the results from retrievals—*Ref.*—to the

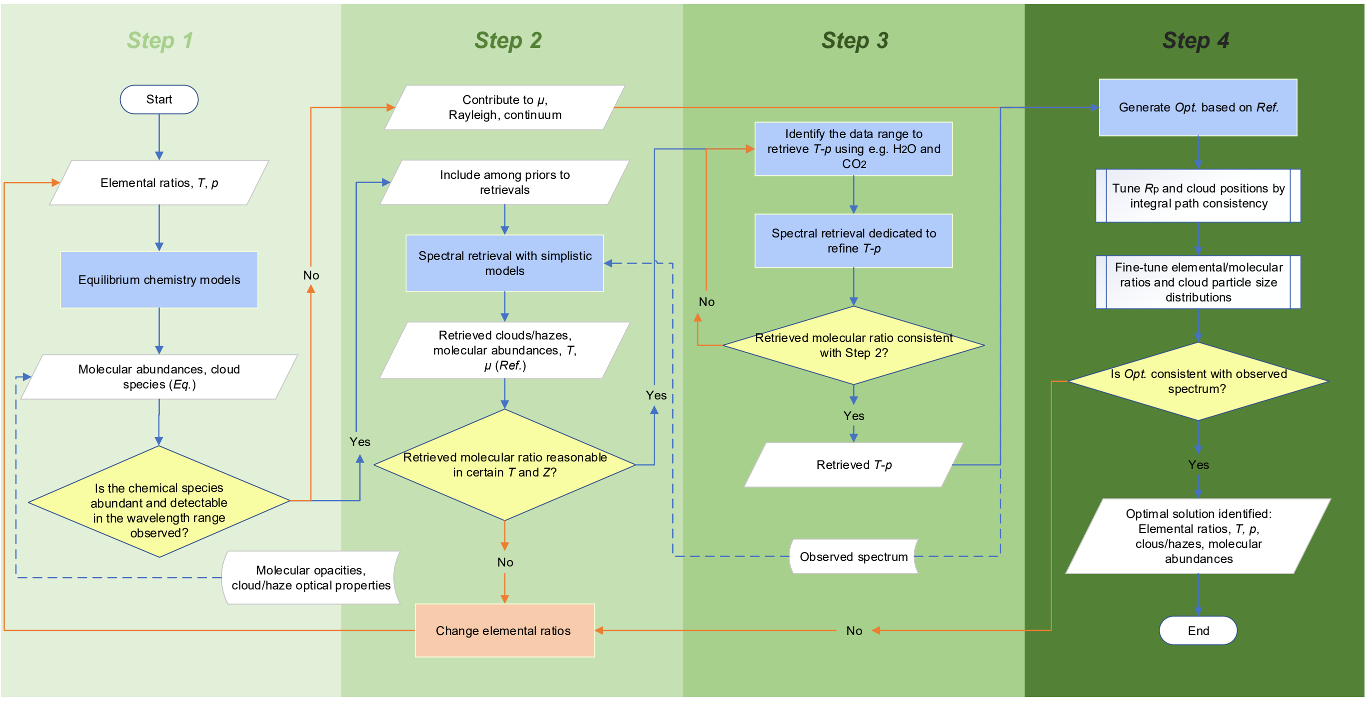

**Figure 2.** Sketch of the approach to analyze exoplanet transit data adopted in this paper.

ones from *Eq.*: if they do not match, we change the assumptions of elemental ratios and/or thermodynamical conditions and repeat the process until convergence is reached (Step 2). To identify optimal solutions—*Opt.*—to explain the observed spectra, we first consider the *T*–*p* profile, which can be refined through retrieval simulations focused on selected spectral bands that contain information about the atmospheric thermal structure (Step 3). After checking the consistency between results from Steps 2 and 3, we finally use the optimal atmospheric thermal profile from Step 3 to better constrain the chemical environment identified in Step 2, including condensates from equilibrium chemical models (Step 4).

We note that the approach adopted in Steps 3 and 4 cannot guarantee the uniqueness of the optimal solutions found. We explain the key steps of our approach in the following sections.

### *2.3.1. Preselection of Chemical and Cloud Species as Priors to Retrievals (Step 1)*

To identify the most abundant molecular species within the expected temperature and metallicity ranges, we start by assuming the atmosphere to be in chemical equilibrium. We used the `GGChem` model integrated into `TauREx 3` to identify the chemical species and their expected abundances. Elements used in the simulations include H, He, Li, C, N, O, F, Na, Mg, Al, Si, P, S, Cl, K, Ca, Ti, V, Cr, Mn, Fe, Ni, Zr, and W (P. Woitke et al. 2018) with the elemental ratios of the outer solar convection zone, mainly derived from spectroscopy of the solar photosphere, as provided by K. Lodders (2021). For the preselection of the chemical species, we have run the simulations with metallicities ranging from 0.01 to 100× solar.

In Step 1, instead of simulating condensations with `GGChem` in the broad parameter space considered, we compared the condensation curves of relevant cloud species at different metallicities occurring in the *T*–*p* regime of WASP-39 b (see Figure 10 in P. Woitke et al. 2018) to exclude cloud species that are unlikely to form in the atmosphere of WASP-39 b. $MgSiO_3$ and $SiO_2$ are the most common condensable species forming in the atmosphere of WASP-39 b in our estimations.

### *2.3.2. Free Retrieval Simulations (Step 2)*

As input to the free retrieval simulations, we adopted the values of planetary and stellar parameters reported by F. Faedi et al. (2011); we started by assuming an isothermal *T*–*p* profile. The chemical priors identified in Step 1 were organized into two sets, as detailed in Table 2: we define the active/inactive gases as the molecules in the gas phase being radiatively active/inactive in the relevant wavelength range.

We narrowed the list of chemical species from Step 1 to a subsample selected according to their contributions to the atmospheric opacity, either because of their predicted abundance at the equilibrium or because of the strengths of their molecular/atomic transitions in the wavelength range observed by JWST. Opacity data for 80 species were sourced from the ExoMol database[4] (K. L. Chubb et al. 2021; J. Tennyson et al. 2024). The versions of cross sections used in this work and the references align with K. L. Chubb et al. (2024). Among the key opacities used in our simulations and plots, we should mention: SiO (S. N. Yurchenko et al. 2022), $CO_2$ (S. N. Yurchenko et al. 2020), $H_2O$ (O. L. Polyansky et al. 2018), Na (N. F. Allard et al. 2019), K (N. F. Allard et al. 2016), NaH (T. Rivlin et al. 2015), CO (A. S. Polanski et al. 2022), $CH_4$ (S. N. Yurchenko et al. 2024), PN (M. Semenov et al. 2025), PO (L. Prajapat et al. 2017), TiO (L. K. McKemmish et al. 2019), VO (L. K. McKemmish et al. 2016), SiS (A. Upadhyay et al. 2018), PS (L. Prajapat et al. 2017), NaOH (A. Owens et al. 2021), $H_2S$ (A. A. A. Azzam et al. 2016), $NH_3$ (P. A. Coles et al. 2019), $PH_3$ (C. Sousa-Silva et al. 2014), $SO_2$ (D. S. Underwood et al. 2016), and HS (M. N. Gorman et al. 2019).

---

[4] https://www.exomol.com/

**Table 2**
Parameter Definitions and Priors of Spectral Retrieval Experiments in Steps 2 and 3 (If Shown in Posteriors)

| Parameter | Definition | Unit | Mode | Priors |
|---|---|---|---|---|
| $R_p$ | Distance from planet center to atmosphere base | $\mathcal{R}_{\rm Je}^{N}$ | factor | 0.80–1.80 |
| $T$ | Atmospheric isothermal temperature (Step 2) | K | linear | 500–2000 |
| $T_{\rm surf}$ | Atmospheric temperature at 10 bar (Step 3) | K | linear | 500–3000 |
| $T_{\rm top}$ | Atmospheric temperature at $10^{-8}$ bar (Step 3) | K | linear | 500–3000 |
| $T_1$ | Atmospheric temperature at $10^{-2}$ bar (Step 3) | K | linear | 500–3000 |
| $T_2$ | Atmospheric temperature at $10^{-4}$ bar (Step 3) | K | linear | 500–3000 |
| $T_3$ | Atmospheric temperature at $10^{-6}$ bar (Step 3) | K | linear | 500–3000 |
| $X_{\rm H_2O}$ | VMR of $H_2O$ | ⋯ | log | $10^{-12}$–$10^{-1}$ |
| $X_{\rm CO_2}$ | VMR of $CO_2$ | ⋯ | log | $10^{-12}$–$10^{-1}$ |
| $X_{\rm SiO}$ | VMR of SiO | ⋯ | log | $10^{-12}$–$10^{-1}$ |
| $X_{\rm Na}$ | VMR of Na | ⋯ | log | $10^{-12}$–$10^{-1}$ |
| $X_{\rm K}$ | VMR of K | ⋯ | log | $10^{-12}$–$10^{-1}$ |
| $X_{\rm CO}$[a] | VMR of CO | ⋯ | log | $10^{-12}$–$10^{-1}$ |
| $X_{\rm N_2}$[a] | VMR of $N_2$, representing heavy-inactive gases | ⋯ | log | $10^{-12}$–$10^{-1}$ |
| $X_{\rm Li}$[a] | VMR of Li, representing light-inactive gases | ⋯ | log | $10^{-12}$–$10^{-1}$ |
| $r_{\rm HPS}$ | HPS cloud particle size | m | log | $10^{-7}$–$10^{-4}$ |
| $N_{\rm HPS}$ | HPS cloud particle number density | $m^{-3}$ | log | $10^{0}$–$10^{8}$ |
| $p_{\rm HPS,deck}$ | HPS cloud deck pressure | Pa | log | $10^{-1}$–$10^{4}$ |
| $p_{\rm HPS,base}$ | HPS cloud base pressure | Pa | log | $10^{-1}$–$10^{4}$ |
| $p_{\rm gray}$ | Gray cloud deck pressure | Pa | log | $10^{-1}$–$10^{4}$ |

**Notes.** VMR represents the volume mixing ratio. HPS represents homogeneous particle size clouds.
[a] Retrieved parameters in nonreference model experiments.

The ExoMol database offers cross sections at a resolving power of $1.5 \times 10^4$ and *k*-tables for the wavelength range of 0.3–50 $\mu$m, which can be directly used by `TauREx 3` and many other retrieval models. In addition, we also included CIA and Rayleigh scattering. For CIA, we took opacity data for $H_2$–$H_2$ and $H_2$–He pairs from the HITRAN database (T. Karman et al. 2019).[5] The Rayleigh scattering estimates for $H_2$, He, $H_2O$, and $CO_2$ were taken from A. N. Cox (2015).

To simulate the impact of clouds/hazes in the retrievals, we adopted the HPS model to provide a first-order representation of the upper cloud layers, which empirically have smaller optical densities than the deeper layers. We added the contribution of gray clouds to mimic the optically thick cloud layers, as caused by large cloud particle size and/or number density in more complex models. With the addition of gray clouds, the retrieval analysis can focus on exploring the contribution of the smaller particles. Refractive indices of different types of $MgSiO_3$ clouds and temperature conditions at which these can form are available in the literature (e.g., C. Jaeger et al. 1994; J. Dorschner et al. 1995; A. Scott & W. W. Duley 1996; C. Jaeger et al. 1998; D. Fabian et al. 2000; C. Jäger et al. 2003; S. Zeidler et al. 2015). For our analysis, we chose refractive indices of amorphous silicates from C. Jäger et al. (2003) to estimate their scattering contributions. We chose not to include the absorption estimation for $MgSiO_3$ clouds due to uncertainties linked to the Lorentz-oscillator fit method for amorphous particles in the infrared, especially beyond 8 $\mu$m, as discussed in C. Jäger et al. (2003). Additionally, our decision was influenced by the fact that scattering contributions are more significant at wavelengths shorter than 8 $\mu$m (refer to the original data paper and our simulations in Section 3.4 for more details). The refractive indices of crystalline $SiO_2$ are from S. Zeidler et al. (2013), collected by the HITRAN database. A summary of databases with these refractive indices is provided in K. L. Chubb et al. (2024).

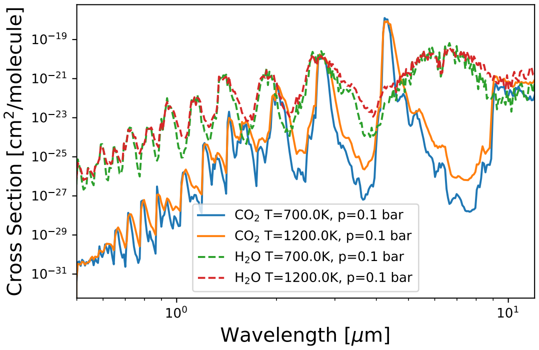

**Figure 3.** Cross sections of $H_2O$ (O. L. Polyansky et al. 2018) and $CO_2$ (S. N. Yurchenko et al. 2020) at two different temperatures at 0.1 bar collected by the ExoMol database.

In addition, we tested the impact of including CO among our priors. We also added the inactive gases $N_2$ and Li as proxies of undetectable species potentially contributing to the atmospheric mean molecular weights ($\mu$) and Rayleigh scattering slopes.

### 2.3.3. Optimization of the Atmospheric Thermal Profile Using Retrieval Techniques (Step 3)

From the posteriors obtained in Step 2, we learned that $H_2O$ and $CO_2$ are key species absorbing in the atmosphere of WASP-39 b. These molecules have cross sections that are very sensitive to the temperature, as showcased in Figure 3, so we can use them to constrain the atmospheric $T$–$p$ profile.

---

[5] https://hitran.org/

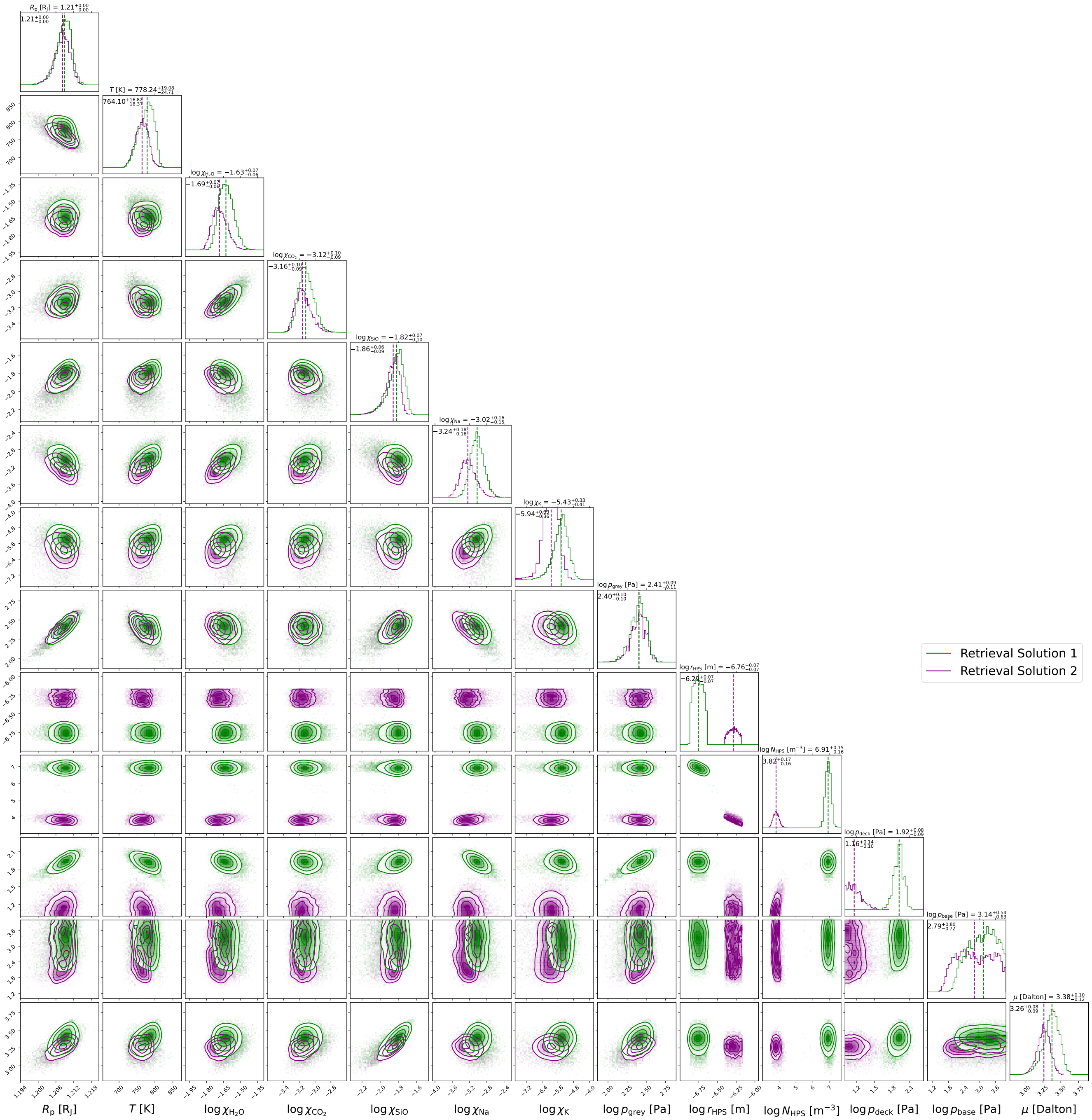

**Figure 4.** Posterior distributions obtained with free retrievals of NIRISS, NIRSpec, and NIRCam spectra (Step 2). We find two islands of solutions (green and purple) originating from the degeneracy of HPS clouds. The numbers above each block represent the median value of the posteriors. The results suggest a significant amount of $H_2O$, SiO, and $CO_2$ in the observable atmosphere. We plot the highest weighted $2 \times 10^4$ traces for visual ease.

### *2.3.4. Optimization of Retrieved Chemical Abundances Including Clouds (Step 4)*

In Step 4, we ran the full equilibrium chemistry model using the *T*–*p* profiles obtained in Step 3 as input. Condensation processes and charges were included in the simulations. Approximately 600 chemical species were estimated by `GGChem` to be present in the atmosphere. However, only a small fraction contributes significantly to the transit spectrum. Others contribute to the atmospheric properties, such as the mean molecular weight. Through retrieval simulations, we converged to the set of molecular abundances and *T*–*p* profiles that better fit the observations and compared them to the predictions of `GGChem` to verify their consistency and estimate the relative abundances of the muted species a posteriori. This last step is important to constrain the metallicity and elemental ratios of the atmosphere.

Given the time gap between the MIRI observations and those obtained with NIRSpec, NIRCam, and NIRISS, we have also conducted a separate cloud particle size distribution optimization that considers only the MIRI observations alongside the homogeneous analysis across the entire spectrum available. For the potential contamination longward 10 $\mu$m

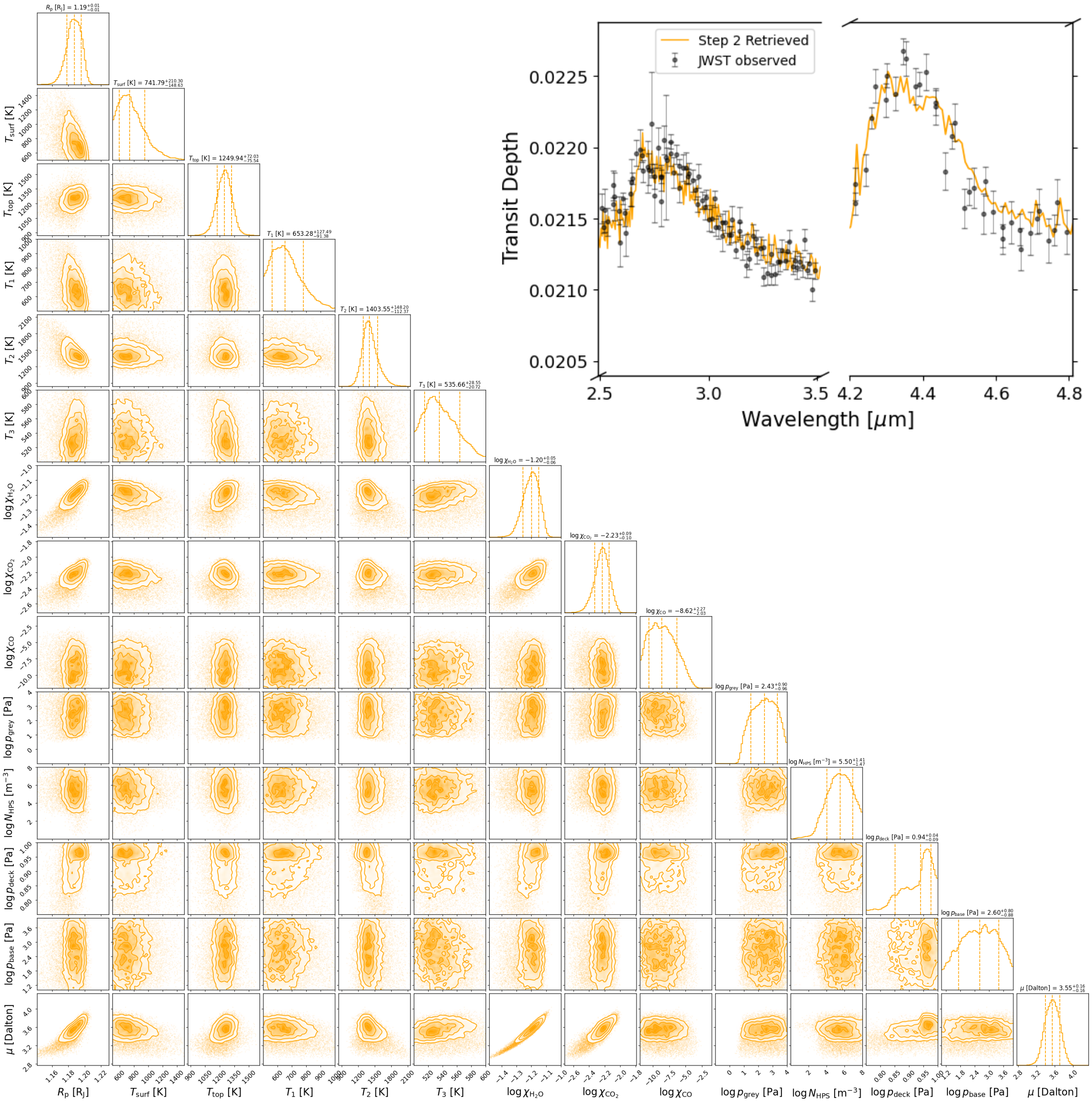

**Figure 5.** Posteriors: the data points selected for retrieving the $T$–$p$ profile and the spectrum fitting in Step 3.

mentioned in Section 1, we have prioritized the observations shortward 10 $\mu$m in model optimization. Our iterative approach, moving from equilibrium chemistry modeling to retrievals and back to equilibrium chemistry modeling, aims to constrain molecular species—in gaseous form or condensed—with prominent spectral features, and then use their molecular abundances as baseline assumptions for deeper analysis with more complex atmospheric models.

### 2.4. Tests on Cloud Particles' Properties and Composition

Concerning the composition of silicate clouds, we have run equilibrium chemistry (`GGChem`) and retrieval simulations to assess whether $MgSiO_3$ (enstatite), $SiO_2$, or $Mg_2SiO_4$ (forsterite) is expected to be the dominant species in the atmosphere of WASP-39 b.

We also conducted sensitivity tests about our assumptions of cloud particles' size distributions and scattering/absorption properties in our simulations. More specifically, we tested the impact of different fractions of absorption/scattering contributions. Scattering and absorption estimates were taken from C. Jäger et al. (2003), assuming $MgSiO_3$ spherical amorphous particles.

In addition, we performed simulations using particle size distributions at each pressure layer adapted from D. Deirmendjian

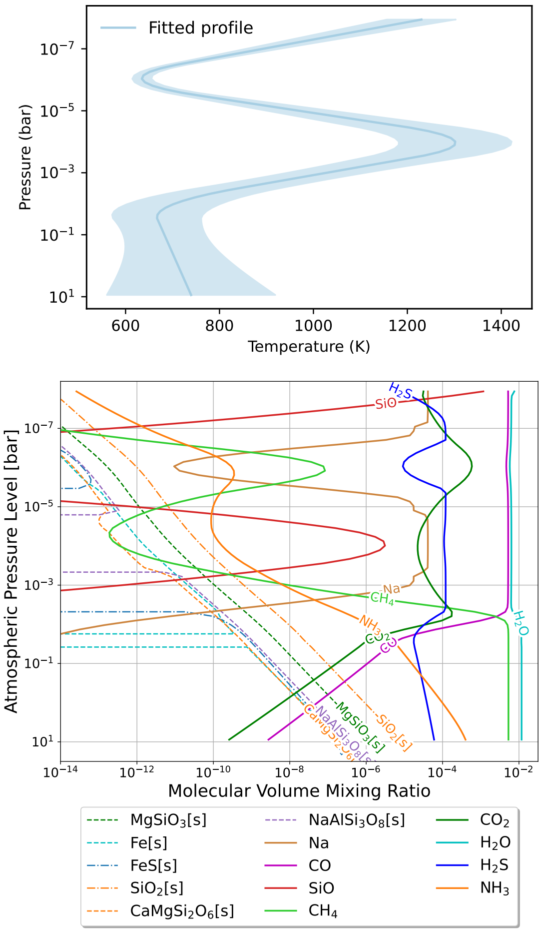

**Figure 6.** Retrieved $T$–$p$ profile (Opt. $T$–$p$) and an example of the most abundant active gas (max. VMR $>10^{-5}$) and condensate species (max. VMR $>10^{-7}$) obtained with GGChem simulations using the median retrieved $T$–$p$ values as input.

(1964):

$$f(n) = \begin{cases} \left(\frac{r_c}{r_{\rm fit}}\right)^a e^{-b\frac{r_c}{r_{\rm fit}}} & \text{if } \ 0 < r_{\rm fit} < 2.7 \\ \left(\frac{r_c - r_t}{r_0}\right)^a e^{-b\frac{r_c - r_t}{r_0}} & \text{if } \ r_{\rm fit} \geqslant 2.7 \end{cases}, \tag{1}$$

where $r_{\rm fit}$ is the best-fit single particle size. We assumed $b = 6$ when $0 < r_{\rm fit} < 2.7$ and $b = 1.5$, $r_0 = 1$, $r_t = r_{\rm fit}\sigma - r_0$, when $r_{\rm fit} \geqslant 2.7$, where $\sigma = 0.7$. We compared the results of these simulations with the assumption of HPSs.

Finally, to test the robustness of our retrieval simulations, we adopted the A–M cloud-microphysics approach available in `YunMa`. We adopted the free convective assumptions (P. Gierasch & B. Conrath 1985) to estimate the eddy diffusion from the mixing length, which is derived from the scaled scale height as described in the A–M approach. The saturation vapor pressure is taken from C. Visscher et al. (2010).

## 3. Results

### 3.1. Selection of Chemical Species for Free Retrievals

The selection process described in Section 2.3.1 (Steps 1 and 2) identifies species that are expected to be abundant according to models assuming chemical equilibrium but also to have large cross sections in the wavelength range probed by JWST, making them the most likely contributors to the transit spectra of WASP-39 b. The active gaseous species playing a major role in our retrieval experiments are: $H_2O$, $CO_2$, SiO, Na, and K. A more comprehensive selection of active chemical species is reported in Appendix A. We also report there how molecular abundances change with metallicity and temperature at the relevant pressures probed in the exoplanet atmosphere.

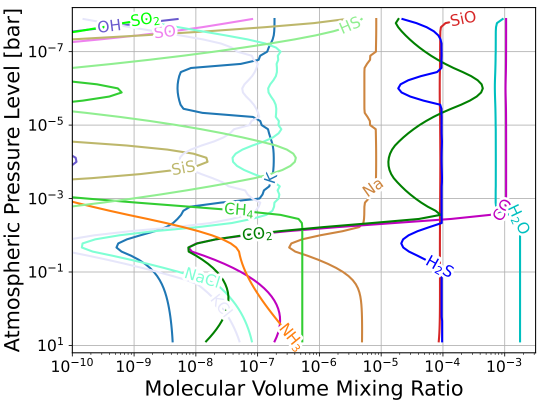

**Figure 7.** Optimized VMRs of the active gases as a function of pressure; these were obtained by fine-tuning the results obtained with GGChem to better reproduce JWST's data. Only the most abundant gases are plotted here for visual ease.

Some gaseous species were excluded from the selection of priors during preliminary retrieval tests because their spectral features are completely masked by other species within a reasonable abundance range, despite being highlighted in the initial selections and showing features similar to those in observations. For example, SiS is predicted to be abundant in the atmosphere of WASP-39 b under chemical equilibrium conditions. However, its spectral features are less prominent than those of other selected species. Only if SiS's abundance exceeded those of $H_2O$ and $CO_2$ by an order of magnitude, an unlikely scenario, would its features become discernible in the transit depth rather than being obscured by other molecular signatures. However, in such a case, SiS would significantly increase the mean molecular weight, reducing the atmospheric scale height and compressing the overall molecular features in a way that is not compatible with the observations.

### 3.2. Free Retrieval Results

In Steps 2 and 3, we performed free retrievals to constrain the gas abundances and thermal profiles. Figure 4 shows the posterior distributions obtained in Step 2, where $T$–$p$ profiles are kept constant. Here, two islands of solutions (Solutions 1 and 2) are found, stemming from the degeneracy of the $MgSiO_3$ HPS clouds. Both retrieved solutions fit the observed spectrum with no statistical preference, as suggested by their Bayesian evidence. Despite the apparent degeneracy, the gas-phase species' abundances in the two cloud solutions are consistent. While the cloud particle radius in Solution 2 is larger than in Solution 1, the particle number density is 3 orders of magnitude lower. As a result, the opacity density of the HPS cloud in Solution 2 is lower, but it is still detectable in transit due to its high altitude. We show the spectral fit and optical depth details of the optimized retrieval in Appendix B. Test cases where CO or muted species ($N_2$ or Li) are displayed in Appendix C.

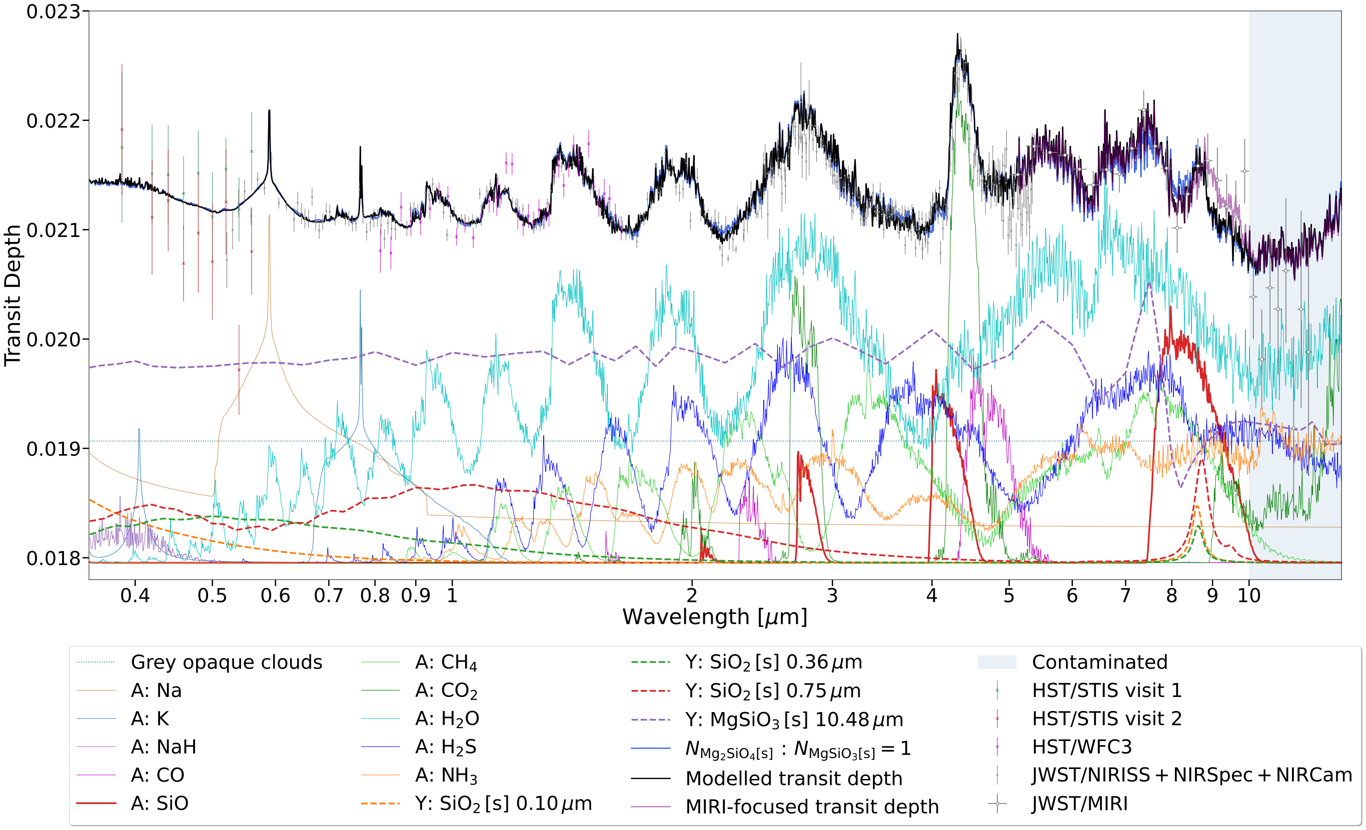

**Figure 8.** Best fit to the JWST spectral data (black and purple lines at the top). *A*: individual gas-phase absorption, *Y*: cloud scattering and absorption (if taken), assuming specific cloud particle radii in the simulations. We only plotted the most significant opacity contributors for visual ease, where opacities of low-abundance species, including $SO_2$, are included in the calculation but are not shown in the plot. Rayleigh scattering and CIA are not shown for the same reason. NIRISS, NIRSpec, and NIRCam spectral data are taken from A. L. Carter et al. (2024), MIRI data from D. Powell et al. (2024), and STIS and WFC3 data from A. Saba et al. (2025). Details of the data used and offsets adopted here are described in Section 2.1. Beyond 10 $\mu$m, the MIRI spectrum is potentially contaminated according to L. Flagg et al. (2024).

From the free retrievals in Step 2, we determined that the 2.5–3.5 and 4.2–4.8 $\mu$m spectral windows—where $H_2O$ and $CO_2$ exhibit strong absorption—are the most informative for further constraining the *T*–*p* profile, because these are the dominant species shaping the overall spectrum and their spectral lines are highly temperature-sensitive. We show in Figure 5 the detailed retrieval results of this step and Figure 6 the optimal *T*–*p* profile as retrieved in Step 3 and an example of `GGChem` simulations with condensates using the optimal *T*–*p* profile as input.

### 3.3. Optimal Solutions to Webb Data

Figure 7 shows the abundances of the gaseous species as a function of pressure for the optimal solution: these were obtained by fine-tuning the results obtained with GGChem to better reproduce Webb's data. Only the volume mixing ratios (VMRs) of the most abundant active gases are shown in Figure 7. The optimal solution in the gas phase corresponds to the following elemental ratios: $2.27 \times \mathrm{O/H}$, $1.39 \times \mathrm{C/H}$, $1.67 \times \mathrm{Si/H}$, $3.35 \times \mathrm{S/H}$, $2.06 \times \mathrm{Na/H}$, $0.55 \times \mathrm{K/H}$ with respect to the solar abundance ratios from K. Lodders (2021).

In addition to the gaseous species, we have found that HPS clouds of multiple particle sizes are needed for an optimal fit. In our simulations, we have included three particle sizes for $SiO_2$, i.e., 0.01, 0.4, and 0.8 $\mu$m, and one for $MgSiO_3$ clouds, i.e., 10 $\mu$m. The fit to the MIRI data can be improved if we use 1 $\mu$m particle size for $SiO_2$ while keeping the $MgSiO_3$ particle size.

In Figures 8, 9, 1,0 and 11, the final simulated spectra are plotted against the data. Figure 12 presents the opacities along the optical paths, together with the atmospheric properties of each pressure layer in the observed atmosphere.

### 3.4. Cloud Particles' Properties and Composition: Consistency with Laboratory Measurements and Microphysics Models

GGChem chemical equilibrium simulations suggest a correlation between the Si:O ratio and the relative abundances of enstatite versus forsterite. Subsolar Si/O prefers the formation of enstatite over forsterite. In addition, enstatite provides a better fit to the observations, as shown in Figures 8 and 9, in agreement with Si/O ~0.7 as suggested in this work.

Furthermore, we tested the impact of different fractions of absorption/scattering contributions for enstatite clouds, as described in Section 2.4, and show the results in Figure 13 (green, yellow, and light-blue spectra). In addition, we compared simulations using the particle size distributions described in Section 2.4 with those assuming HPSs. The results are reported in Figure 13 (black and light-blue spectra). These results show good agreement with the results using HPS clouds shown in Figures 7 and 8.

To test the robustness of our retrieval simulations with respect to atmospheric dynamics, we adopted the cloud-

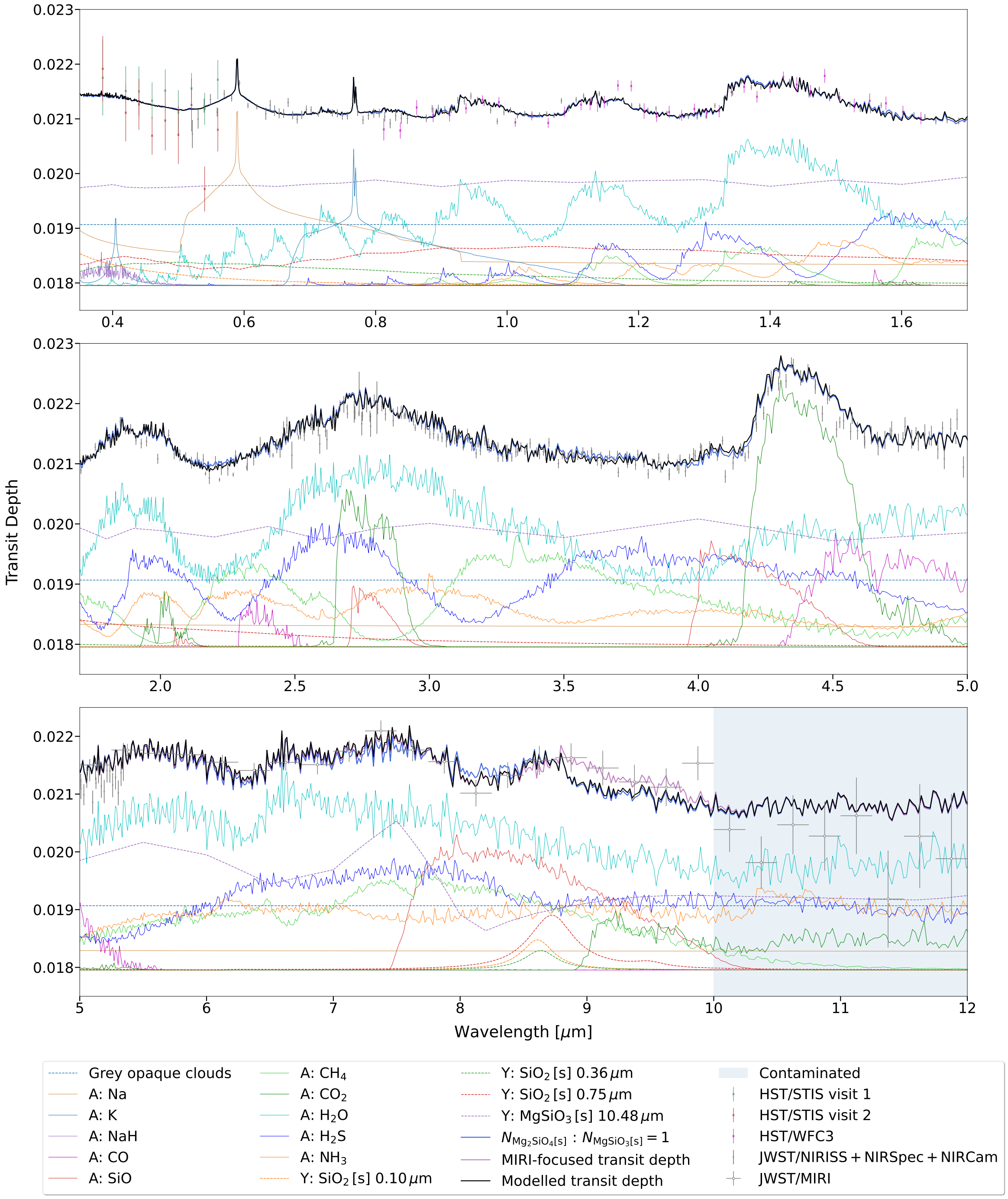

**Figure 9.** Zoom-in of Figure 8 in different spectral windows. Here, the $x$-axis of each subplot is displayed on a linear scale.

microphysics approach described in Section 2.4. SiO and cloud mixing ratios derived from this approach are shown in Figure 14, and the other molecular mixing ratios are shown in Figure 15. The simulations, with assumed values of the sedimentation coefficient $f_{\rm sed}$, align with the former observation-driven results. We compared the mean molecular mixing ratios of the clouds and found consistency between the HPS model constrained by observations and those simulated theoretically using the A–M approach, as shown in Figure 14. We used the chemical mixing profile with the SiO VMR from the A–M approach and plotted the simulated spectrum against the observations in Figure 16.

## 4. Discussion

### 4.1. Silicon versus Sulfur Chemistry to Explain JWST Spectra of WASP-39 B

The previous literature suggested $SO_2$ as an explanation of the features at 4.1, 7.7, and 8.5 $\mu$m (see Section 1.3 and Figure 17). While we are not excluding the presence of $SO_2$, we propose here that the spectral feature observed at 4.1 $\mu$m is mainly caused by SiO (Figure 10) and the features at 7.7 and 8.5 $\mu$m can be explained by silicate clouds (Figure 11). To be clearer, we compared the transit depths simulated with different amounts of SiO in Figure 18. Results from

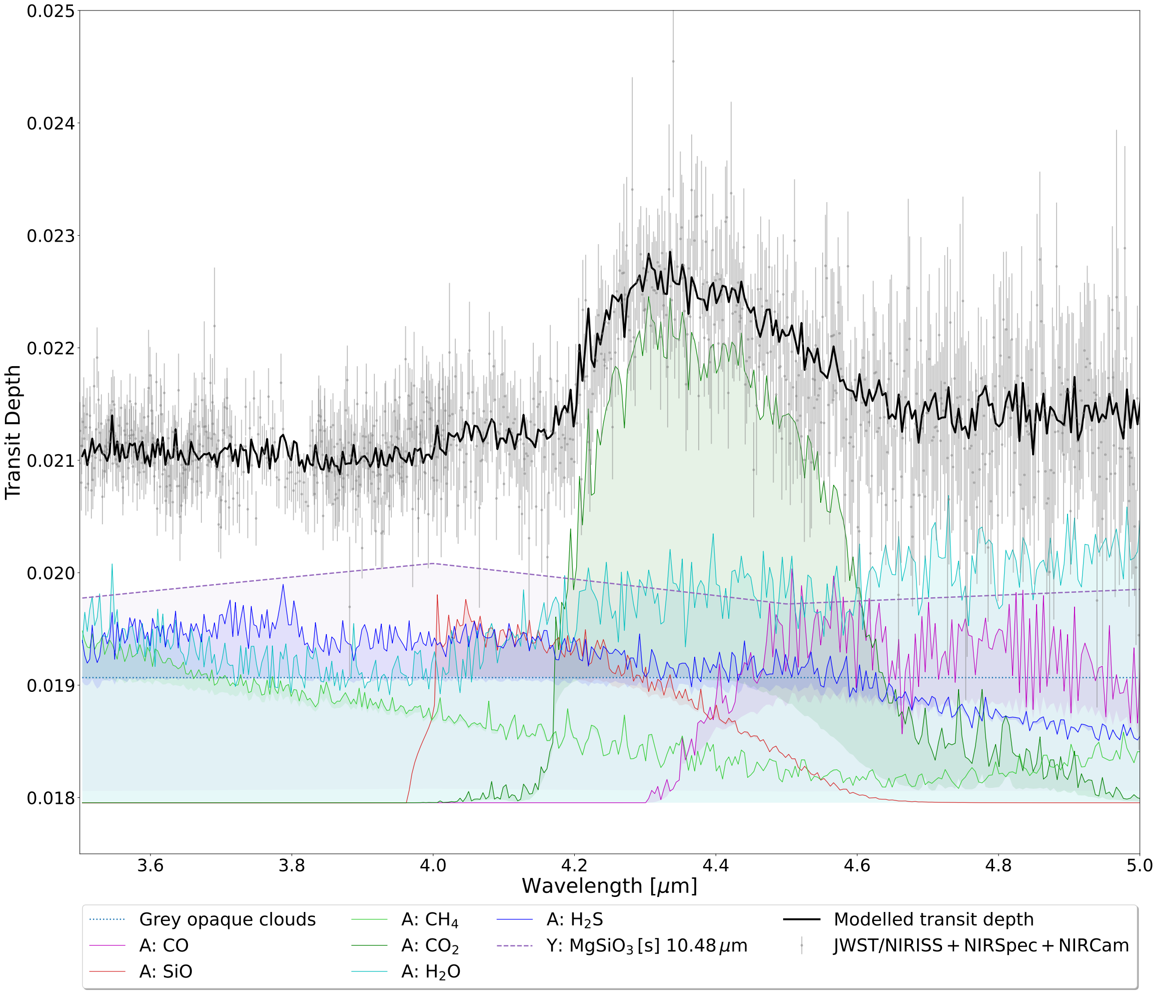

**Figure 10.** Zoom-in around 4.1 $\mu$m of Figure 8. The model is compared with the native-resolution observations (gray data points with error bars). We show the individual molecular contributions (colored) of the optimized case (black). To reveal their altitude dependence, we plot as shaded areas the gas-phase molecular absorptions integrated from $10^{-1}$ bar to the top of the atmosphere.

our retrieval analyses suggest $H_2O$, $CO_2$, SiO, silicate clouds, Na, and K can fit well NIRISS, NIRSpec, NIRCam, and MIRI observations. Further optimization with both shorter wavelengths and MIRI observations helped to constrain the particle sizes, composition, and location of silicate clouds. The presence and abundances of both gas and condensate species are compatible with a scenario of chemical equilibrium at the temperatures expected for this planet.

### 4.2. Self-consistency with Equilibrium Chemistry and Condensation

Chemical equilibrium simulations that do not account for condensation represent an extreme case, where the gas-phase molecules remain abundant in the atmosphere; in other words, gas-phase molecules supersaturate instead of condensing out. By contrast, chemical equilibrium simulations including condensation represent another extreme case, as they predict maximum depletion from condensation processes. In the simulations performed as part of this study with `GGChem`, assuming condensation, multiple species of silicate form, with $MgSiO_3$ and $SiO_2$ having the highest abundance in the observable atmosphere.

We have further investigated self-consistency using one-dimensional, physically motivated models (see Section 3.4). These results demonstrate a high degree of consistency with those presented in Section 3.2; however, they are limited by the assumption of the one-dimensional parameterization.

Additional complexity arises from uncertainties in cloud particle materials, forms, shapes, and size distributions. A more detailed understanding of the annealing and crystallization processes might be needed to fully grasp the cloud microphysics and properties. However, we defer these aspects to future studies, pending more advanced laboratory and observational data from both within and beyond the solar system.

#### 4.2.1. Cloud Properties in Retrievals

Our retrieval simulations have indicated that gas-phase species alone may not account for the observed opacity in the optical and infrared wavelength range. While clouds can explain the missing opacity, they also represent a complex challenge for atmospheric characterization, requiring significantly higher statistical and computing capabilities. Studies that include clouds need to balance the trade-offs between parametric/characteristic models and more complex microphysics models. There have been efforts to model

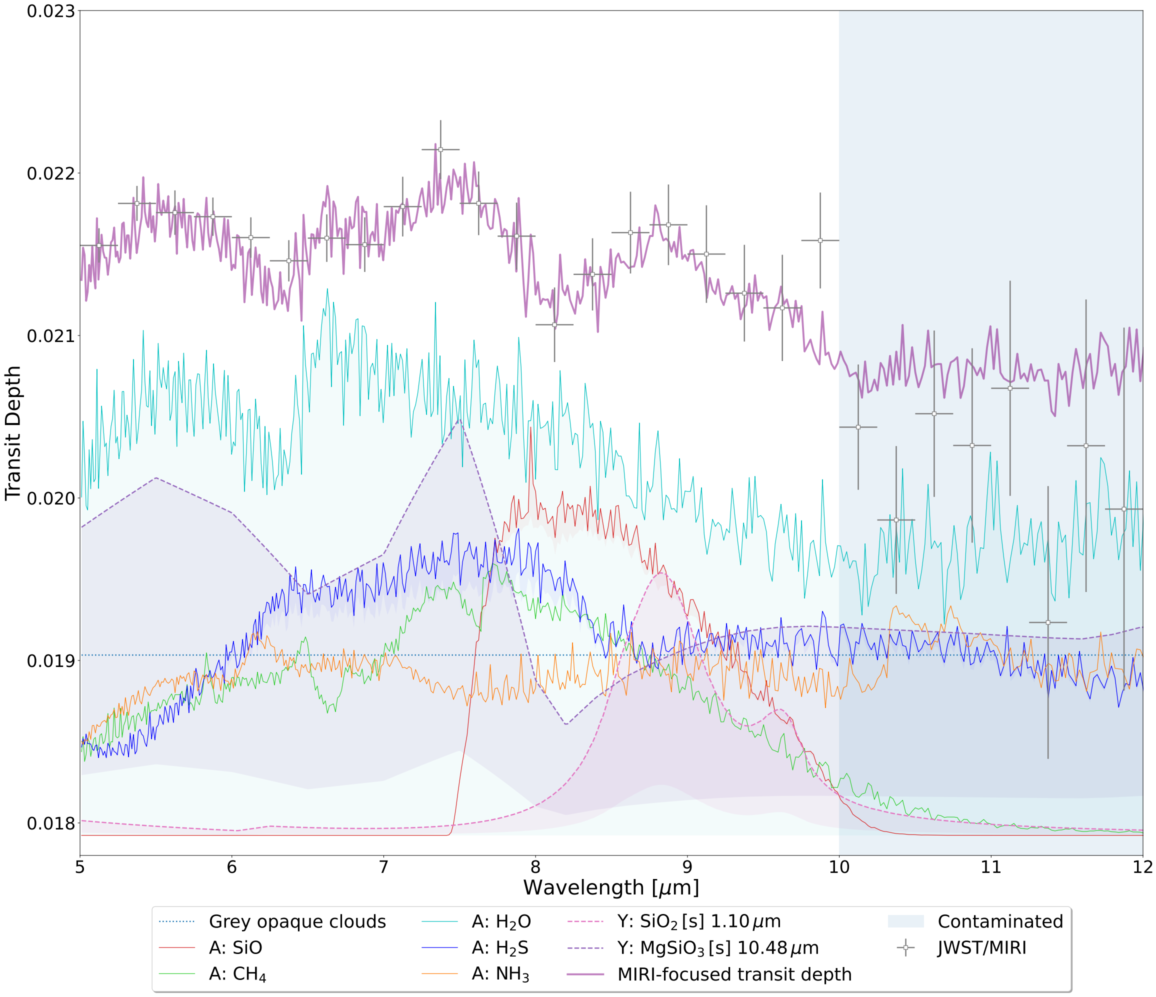

**Figure 11.** Zoom-in of the MIRI window of the MIRI-focused fit in Figure 8. We plot as shaded areas the gas-phase molecular absorptions integrated from $10^{-3}$ bar to the top of the atmosphere.

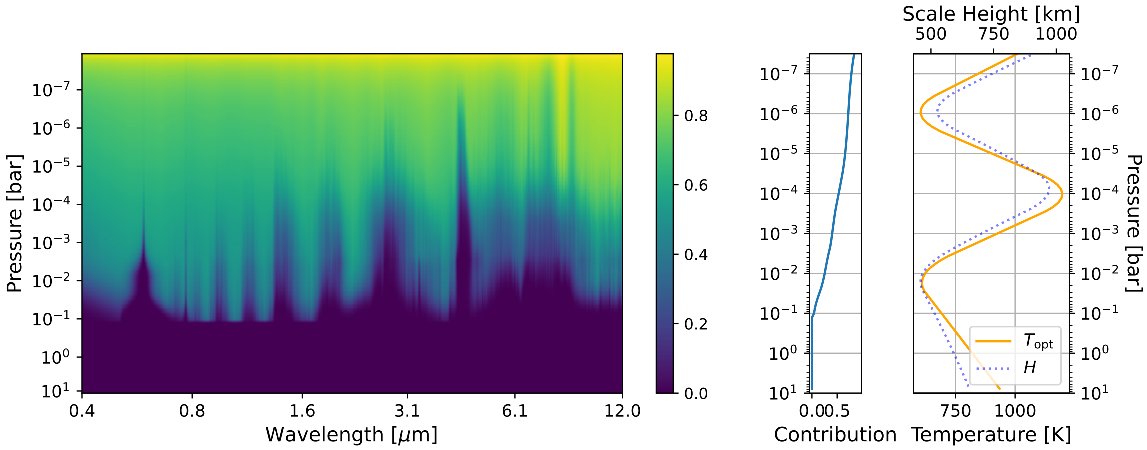

**Figure 12.** Estimated optical depths through optical paths centered at each pressure level (left panel), wavelength-normalized opacity contributions (central panel), adopted temperature profile, and estimated scale heights (right panel).

cloud formation on WASP-39 b, as discussed by A. Arfaux & P. Lavvas (2024), who compared cloud models of varying complexity, highlighting their respective strengths and limitations. However, due to the uncertainties in the underlying atmospheric chemistry and dynamics, key aspects of the cloud properties on WASP-39 b, such as cloud composition and size distribution, remain ambiguous. Detailed parameters like particle shapes, contact angles, and surface tension are beyond the reach of current observational capabilities. Therefore, an optimal strategy for interpreting the available data is to begin with simplified cloud models in retrievals, allowing optimized flexibility in particle size distributions. More advanced cloud retrieval methods, such as those proposed by S. Ma et al. (2023), are

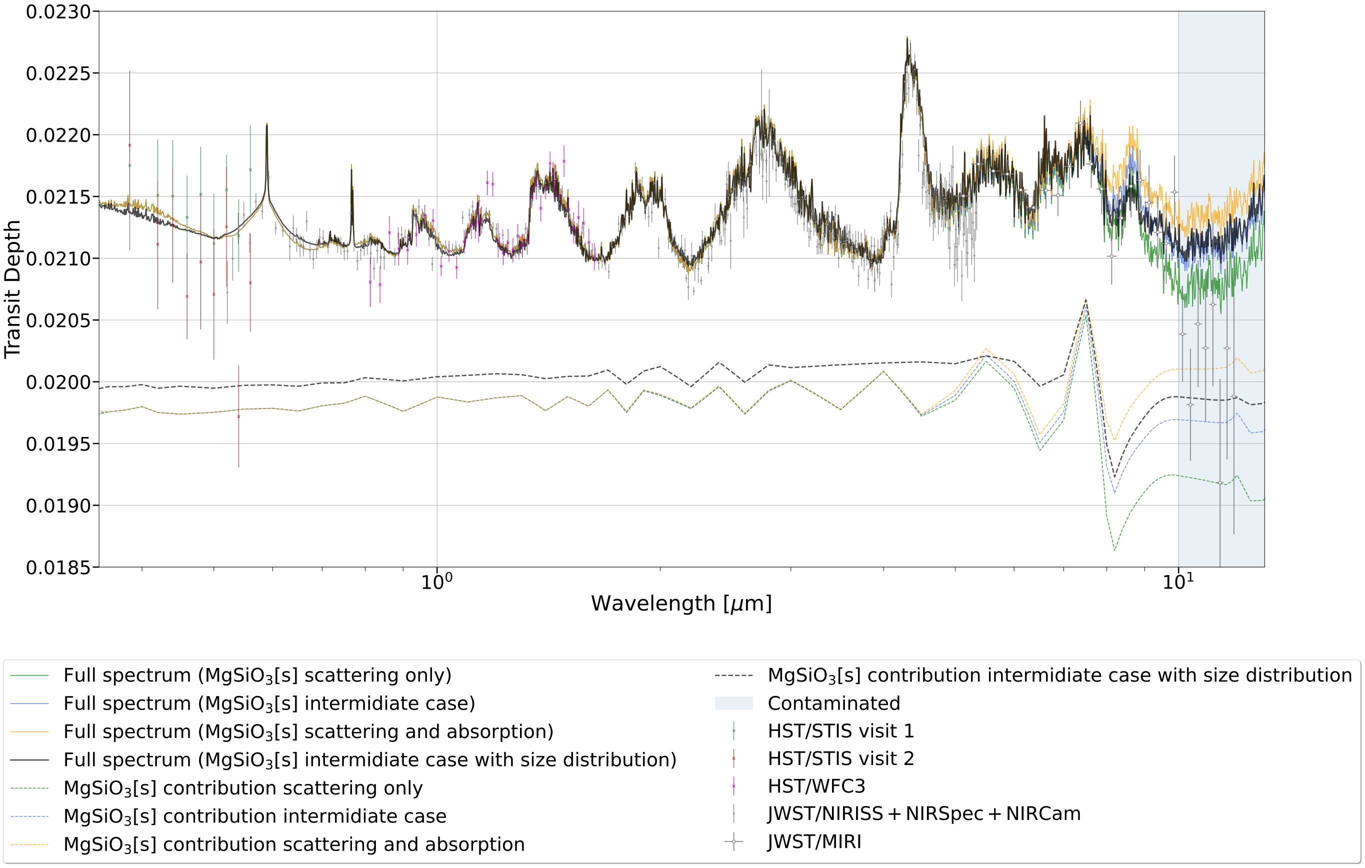

**Figure 13.** Spectra estimated with different cloud absorption/scattering contributions and particle size distributions. Green: reference model as shown in Figure 8 with the HPS cloud model, and only the scattering contribution is included. Yellow: HPS clouds with scattering and absorption equally represented. Light blue: intermediate case between the yellow and green cases. Black: similar to the light-blue model but with particle size distribution following Equation (1) adapted from D. Deirmendjian (1964) at each pressure layer. Scattering and absorption estimates were taken from C. Jäger et al. (2003).

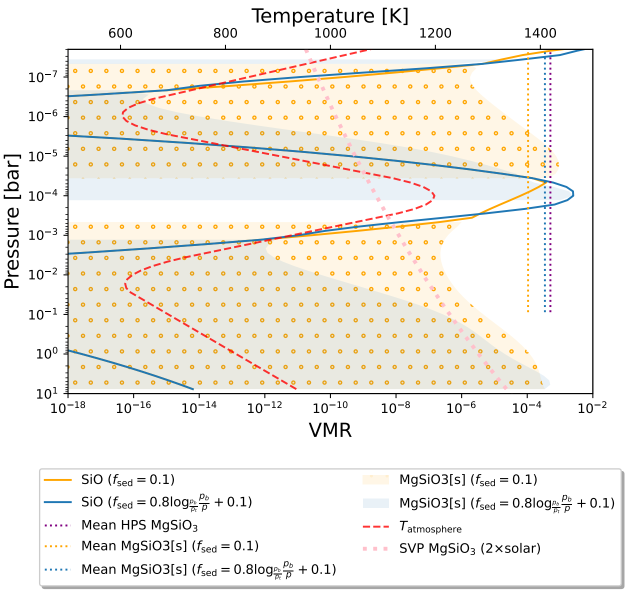

**Figure 14.** SiO and cloud mixing ratios derived from the cloud microphysics approach as described in A. S. Ackerman & M. S. Marley (2001) and available in `YunMa`. We also show the mean VMR (dotted lines) of the $MgSiO_3$ clouds constrained by observations with the HPS model and by the molecular draft balance, with two assumptions of the sedimentation efficiency ($f_{sed}$). The mean VMR is estimated above the gray cloud deck (refer to the saturated layer across all the wavelengths in Figure 12, left panel).

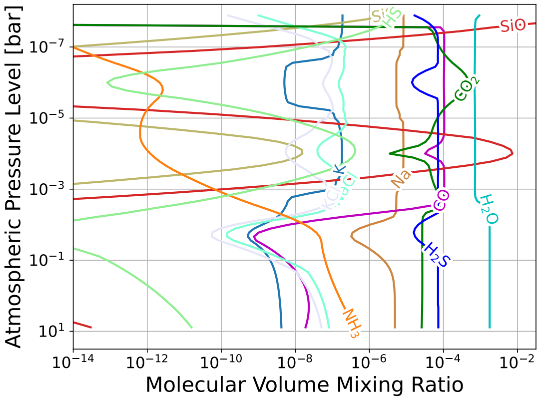

**Figure 15.** Similar to Figure 7 but optimized for the SiO profile shown in Figure 14.

theoretically feasible but are better suited for follow-up studies once a more precise understanding of the basic atmospheric chemistry and dynamics is established. By constraining the dimensionality of the models and refining the priors to fit the parameters, our approach allows for more efficient and tailored retrievals. Therefore, as an optimization for the current JWST retrieval studies, we chose to use a characteristic HPS model plus a gray cloud model, as detailed in Section 2.3.2, to start with. We have

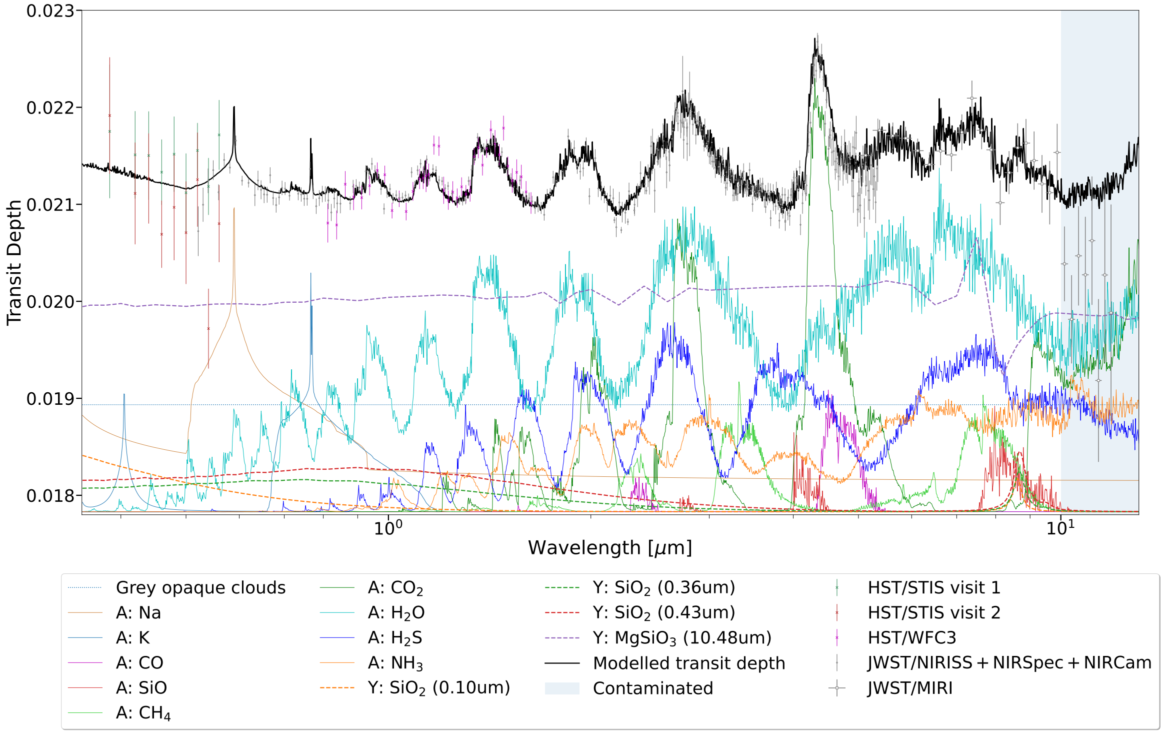

**Figure 16.** Similar to Figure 8, but assuming the chemical profiles shown in Figure 15 and the cloud particle size distribution same as the black spectrum in Figure 13.

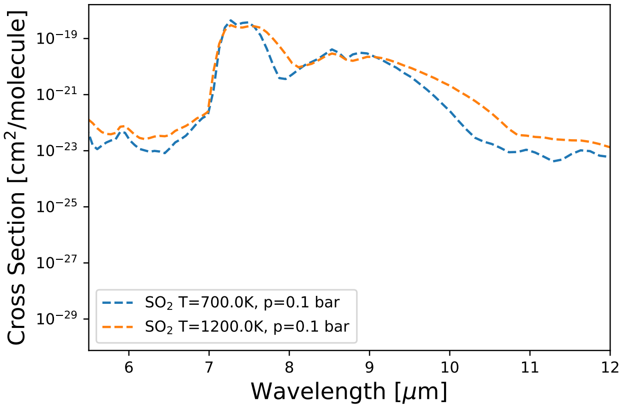

**Figure 17.** Cross sections of $SO_2$ from D. S. Underwood et al. (2016) collected by the ExoMol database.

tested the robustness of these simplistic assumptions by comparing the results in Section 3.2 with those obtained with cloud microphysical models (Sections 2.4 and 3.4). The high degree of consistency between the results obtained with the two different approaches is a good indicator of the plausibility of our assumptions.

### 4.2.2. Optimized Free Retrieval in Step 2

As explained in Section 3.3, the direct indication from retrieval results is the ratios between major tracers. The relative abundances between species determine the shape of the transit depth versus wavelengths. Indirectly, the retrieved results constrain the metallicity and temperature.

Parameters such as the absolute abundances of major tracers may shift due to the exclusion of most of the species (see Sections 2.3.1 and 3.1) during retrieval. These unselected species have two major impacts on the spectrum: their mass tunes the atmospheric scale height, and their cumulative opacities contribute directly to the spectrum's continuum. While the inclusion of a gray cloud model mitigates the latter impact to a certain extent, as a result, the retrieval algorithm adjusts other atmospheric properties, such as density and temperature, to optimize the integration path and maintain the strength of key spectral features.

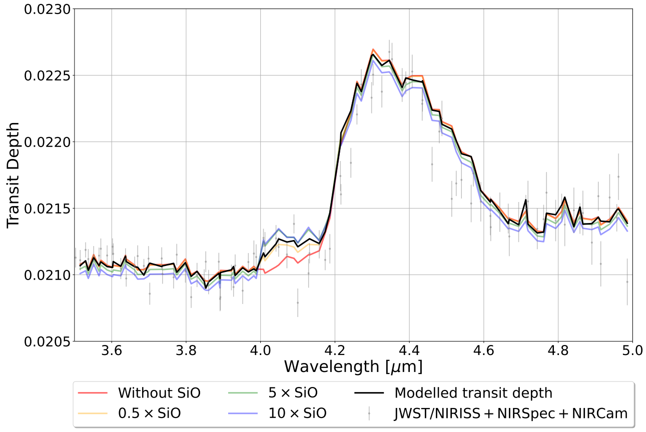

**Figure 18.** Transit depth simulations with varying amounts of SiO, indicating the importance of an optimized VMR of SiO for a good fit with the observed spectrum.

### 4.3. Uncertainties and Suggestions

Attention is needed to select the initial elemental ratios and condensation parameterization. Although certainty cannot be guaranteed, our study relies on accepted knowledge, with sufficient margins to account for uncertainties in thermal profiles, elemental ratios, and condensation processes.

Additionally, more accurate opacity data of varied temperature and pressure could help resolve the degeneracy between temperature, metallicity, and other parameters. However, conducting laboratory experiments under conditions that replicate those found in extraterrestrial environments remains challenging.

As the reported values for the atmospheric properties are sensitive to and heavily dependent on atmospheric model assumptions—including the species considered in the chemistry and opacity—we highlight the importance of clarifying in models the molecular species assumed:

1. in calculating the basic atmospheric properties, e.g., mean molecular weight;
2. as opacity sources contributing to the transit depth;
3. in deriving the elemental ratios to facilitate easier understanding and comparison of results in future work.

In addition, some misunderstanding of literature values may stem from different definitions of metallicity. In this paper, we followed the definitions summarized by N. R. Hinkel et al. (2022; see also the review by M. R. Swain et al. 2024). We report the values of the total volume fraction for all elements other than $H_2$ and He relative to solar and report the elemental ratios to H directly in the final results. For the benefit of future work in the field, we advocate for clarity in specifying the reference and which elemental abundance (e.g., solar outer convective zone or protostellar disk) is being used, whether in mass ratios or volume ratios, linear or log scales, solar units or absolute values, when referring to the term “metallicity.”

## 5. Conclusions

We have studied the chemical composition and cloud/haze formation in the atmosphere of WASP-39 b, using recent JWST spectroscopic and transit observations of this planet to inform our hypotheses and models. For this work, we have used a novel, hybrid approach that combines multistep, free retrieval simulations using the results of equilibrium chemistry models and cloud microphysics to constrain the priors.

Our analysis suggests that, in addition to $H_2O$, $CO_2$, Na, and K, already identified in previous works in the literature, silicon-based chemistry plays a major role in shaping the chemistry and condensates of the atmosphere of WASP-39 b. Our Bayesian retrievals strongly support the presence of the gas-phase SiO together with $MgSiO_3$ and $SiO_2$ clouds to explain the observed spectral features around 4.1, 7.5, and 8.8 $\mu$m. This scenario is compatible with results from equilibrium chemistry models. $H_2O$ and $CO_2$ absorptions in the 2.5–3.5 and 4.2–4.8 $\mu$m spectral windows were used to constrain the thermal profile as a function of pressure.

Previous literature suggested $SO_2$ as an explanation of the features at 4.1, 7.7, and 8.5 $\mu$m, where the $SO_2$ formation was explained by potential photochemical processes. Meanwhile, it is important to explore alternative scenarios. As current models of chemical disequilibrium and photochemistry are inevitably limited by the elements considered and the size of the chemical network (see, e.g., R. Veillet et al. 2026), we adopt here equilibrium chemistry simulations to include a more comprehensive list of elements as initial conditions.

Our optimal solution in the gas phase corresponds to the following elemental ratios: $2.27 \times \mathrm{O/H}$, $1.39 \times \mathrm{C/H}$, $1.67 \times \mathrm{Si/H}$, $3.35 \times \mathrm{S/H}$, $2.06 \times \mathrm{Na/H}$, $0.55 \times \mathrm{K/H}$ with respect to the solar abundance ratios from K. Lodders (2021). In addition to the gaseous species, our optimal solution includes three particle sizes for $SiO_2$, i.e., 0.01, 0.4, and 0.8 $\mu$m, and one for $MgSiO_3$ clouds, i.e., 10 $\mu$m. The fit to the MIRI data can be improved if we use 1 $\mu$m particle size for $SiO_2$ while keeping the $MgSiO_3$ particle size.

While the solution proposed here is able to faithfully match all JWST and HST data, we are not in a position to claim its uniqueness, as the method adopted does not comprehensively scan the parameter space of possible chemical species—in gas or solid/liquid phase—and thermodynamical conditions. However, our hybrid approach that combines optimized free retrievals and complex forward models offers higher flexibility and robustness to interpret spectroscopic data compared to previous efforts. For instance, it leverages Bayesian statistics for the sampling algorithm to search for solutions based on observational data, while minimizing biases from prior scientific knowledge. In addition, self-consistent atmospheric models allow for limiting the number of implausible scenarios considered by free retrievals, by constraining the priors with physically informed models.

To further investigate and confirm the chemical and elemental composition of the atmosphere of WASP-39 b, additional spectroscopic data, such as very high-spectral resolution data from the ground aimed at detecting $SO_2$ and SiO, would be needed.

## Acknowledgments

This work is based on observations made with the NASA/ESA/CSA James Webb Space Telescope. The data were obtained from the Mikulski Archive for Space Telescopes at the Space Telescope Science Institute, which is operated by the Association of Universities for Research in Astronomy, Inc., under NASA contract NAS 5-03127 for JWST. These observations are associated with program JWST-ERS-01366 and JWST-DD-2783. The specific observations presented can be accessed via doi:10.17909/qvjr-xx74. This work was supported by the Science and Technology Facilities Council [grant numbers UKRI3305 and UKRI1234]. S.M. and G.T. are thankful for the support from UKSA grants ST/X002616/1 and ST/W00254X/1. S.Y. thanks the STFC Project No. ST/Y001508/1. This project has received funding from the European Research Council (ERC) under the European Union’s Horizon 2020 research and innovation program through an Advanced Investigator grant No. 883830 (ExoMolHD). This work utilized the Cambridge Service for Data-Driven Discovery (CSD3), part of which is operated by the University of Cambridge Research Computing on behalf of the STFC DiRAC HPC Facility (dirac.ac.uk). The DiRAC component of CSD3 was funded by BEIS capital funding via STFC capital grants ST/P002307/1, ST/R002452/1, and STFC operations grant ST/R00689X/1. DiRAC is part of the National e-Infrastructure.

*Software*: Python 3.10.0, numpy 1.26.0 (C. R. Harris et al. 2020), scipy 1.14.0 (P. Virtanen et al. 2020), pymultinest 2.12 (J. Buchner et al. 2014), astropy 5.3.4 (Astropy Collaboration et al. 2022, 2018, 2013), numba 0.59.0 (S. K. Lam et al. 2015)

## Appendix A
## Chemical Species Selection in Wide Parameter Space

We conducted the chemical species selection following the methodology described in Section 2.3.1, covering the parameter space expected for WASP-39 b, i.e., assuming temperatures of 700, 900, 1100, 1300, and 1500 K, and volume metallicities of 0.4, 4, 29, and 67 × solar volume metallicity. The metallicity values are estimated from the constant species' abundance cases with molecular VMRs of $10^{-6}$, $10^{-5}$, $10^{-4}$, and $10^{-3}$. To maintain consistency between the equilibrium and homogeneous abundance simulations, we aim to keep the atmospheric metallicity and mean molecular weight within 20 % difference between the two sets of simulations. We list the highlighted species in Table 3. Examples of key molecular abundances as a function of metallicity and temperature are given in Figure 19.

**Table 3**
Highlighted Chemical Species by the Methodology in Section 2.3.1

| VMR[a] | Met.[△] | $T_{\rm eq}$ (K) | Highlighted Species |
|---|---|---|---|
| *Eq.* Profiles | 0.4 | 700 | $CH_4$, Na, $H_2O$, CrH, $PH_3$, $NH_3$, $SiH_4$, $H_2S$, SiO |
| Constant Profiles $10^{-6}$ | 0.4 | 700 | $SiH_4$, $PH_3$, $CO_2$, CrH, Na, $CH_4$, $NH_3$, CO, $H_2O$ |
| *Eq.* Profiles | 0.4 | 900 | $H_2O$, Na, $CH_4$, CrH, $PH_3$, CO, $H_2S$, SiO, $NH_3$, $SiH_4$ |
| Constant Profiles $10^{-6}$ | 0.4 | 900 | $SiH_4$, $PH_3$, CrH, $CH_4$, Na, $NH_3$, $H_2O$, CO, $H_2S$, SiO |
| *Eq.* Profiles | 0.4 | 1100 | $H_2O$, Na, CrH, CO, $CH_4$, $H_2S$, SiO, $NH_3$ |
| Constant Profiles $10^{-6}$ | 0.4 | 1100 | CrH, $CH_4$, Na, $NH_3$, $H_2O$, CO, $H_2S$, SiO |
| *Eq.* Profiles | 0.4 | 1300 | $H_2O$, Na, CO, CrH, $H_2S$, $CH_4$, SiO, $NH_3$ |
| Constant Profiles $10^{-6}$ | 0.4 | 1300 | Cr, CH, N, NH, $H_2$, C, $H_2$, Si, SH |
| *Eq.* Profiles | 0.4 | 1500 | $H_2O$, Na, CO, $H_2S$, SiO, $CH_4$, $NH_3$ |
| Constant Profiles $10^{-6}$ | 0.4 | 1500 | $CH_4$, Na, $NH_3$, $H_2O$, CO, $H_2S$, SiO, SH |
| Eq. Profiles | 4 | 700 | $CO_2$, $CH_4$, Na, $PH_3$, $H_2O$, CrH, K, NaOH, $H_2S$, $NH_3$, SiO, $SiH_4$, CO |
| Constant Profiles $10^{-5}$ | 4 | 700 | $SiH_4$, $PH_3$, $CO_2$, NaOH, $CH_4$, CrH, K, Na, $NH_3$, $H_2O$, CO, $H_2S$, SiO |
| *Eq.* Profiles | 4 | 900 | CaOH, $CO_2$, $H_2O$ Na, CrH, $PH_3$, CO, $CH_4$, K, $H_2S$, SiO, NaOH, $NH_3$, $SiH_4$ |
| Constant Profiles $10^{-5}$ | 4 | 900 | CaOH, $SiH_4$, $PH_3$, $CO_2$, NaOH, $CH_4$, CrH, Na, K, $NH_3$, $H_2O$, CO, $H_2S$, SiO |
| *Eq.* Profiles | 4 | 1100 | CaOH, $CO_2$, $H_2O$ Na, CrH, CO, $PH_3$, K, $H_2S$, MgH, $CH_4$, SiO, $NH_3$, SiS |
| Constant Profiles $10^{-5}$ | 4 | 1100 | CaOH, $CO_2$, $PH_3$, $CH_4$, MgH, CrH, Na, K, $NH_3$, $H_2O$ $H_2S$, CO, PS, SiO, SH |
| *Eq.* Profiles | 4 | 1300 | CaOH, TiO, $H_2O$ $CO_2$, Na, CO, CrH, $H_2S$, MgH, K, $PH_3$, SiO, $CH_4$, $NH_3$, SiS |
| Constant Profiles $10^{-5}$ | 4 | 1300 | CaOH, TiO, $CO_2$, $PH_3$, MgH, $CH_4$, CrH, $NH_3$, Na, K, $H_2O$, PS, $H_2S$, CO, PO, SiO, SH |
| *Eq.* Profiles | 4 | 1500 | TiO, $H_2O$, $CO_2$, Na, CO, MgH, CrH, $H_2S$, K, $PH_3$, SiO, $CH_4$, $NH_3$, SiS, SH |
| Constant Profiles $10^{-5}$ | 4 | 1500 | TiO, $CO_2$, $PH_3$, MgH, $CH_4$, CrH, $NH_3$, Na, K, $H_2O$, PS, $H_2S$, CO, SO, PO, SiO, SH, SiS, AlF |
| Eq. Profiles | 29 | 700 | $CO_2$, $CH_4$, Na, $H_2O$, $PH_3$, CrH, CO, NaOH, K, $H_2S$, SiO, $NH_3$ |
| Constant Profiles $10^{-4}$ | 29 | 700 | $SiH_4$, $PH_3$, NaOH, $CO_2$, $CH_4$, CrH, K, Na, $NH_3$ |
| *Eq.* Profiles | 29 | 900 | CaOH, $CO_2$, $H_2O$, Na, CrH, CO, $PH_3$, K, $H_2S$, $CH_4$, NaOH, SiO, $NH_3$ |
| Constant Profiles $10^{-4}$ | 29 | 900 | CaOH, $SiH_4$, $PH_3$, $CO_2$, NaOH, $CH_4$, CrH, $NH_3$, Na, K, $H_2O$, $H_2S$, |
| *Eq.* Profiles | 29 | 1100 | CaOH, $CO_2$, $H_2O$, Na, CrH, CO, $H_2S$, K, $PH_3$, MgH, NaOH, SiO, $CH_4$, $NH_3$, SiS |
| Constant Profiles $10^{-4}$ | 29 | 1100 | CaOH, $CO_2$, $PH_3$, NaOH, $CH_4$, MgH, CrH, $NH_3$, Na, K, $H_2O$, $H_2S$, PS, CO, PO, SiO |
| *Eq.* Profiles | 29 | 1300 | CaOH, $CO_2$, TiO, $H_2O$, Na, $H_2S$, CO, CrH, MgH, K, $PH_3$, SiO, NaOH, $CH_4$, NaH, $NH_3$, SiS |
| Constant Profiles $10^{-4}$ | 29 | 1300 | CaOH, TiO, $CO_2$, $PH_3$, NaOH, $CH_4$, MgH, CrH, $NH_3$, NaH, Na, K, $H_2O$, PS, $H_2S$, SO, CO, PO, SiO |
| *Eq.* Profiles | 29 | 1500 | $CO_2$, TiO, $H_2O$, Na, CO, $H_2S$, MgH, CrH, K, SiO, $PH_3$, AlO, NaOH, NaH, PS, $NH_3$, $CH_4$, SiS, PO, SH |
| Constant Profiles $10^{-4}$ | 29 | 1500 | TiO, $CO_2$, $PH_3$, AlO, NaOH, $CH_4$, MgH, CrH, $NH_3$, NaH, $SO_2$, Na, K, $H_2O$, PS, $H_2S$, SO, CO, PO, SiO, SH, HF |
| *Eq.* Profiles | 67 | 700 | $CO_2$, $CH_4$, Na, $H_2O$, CrH, $PH_3$, NaOH, CO, K, $H_2S$ |
| *Eq.* Profiles | 67 | 900 | CaOH, $CO_2$, $H_2O$, Na, CrH, CO, $PH_3$, $H_2S$, K, NaOH, $CH_4$, SiO |
| *Eq.* Profiles | 67 | 1100 | CaOH, $CO_2$, $H_2O$, Na, CrH, $H_2S$, CO, K, $PH_3$, MgH, NaOH, SiO, $CH_4$, $NH_3$, NaH |
| *Eq.* Profiles | 67 | 1300 | CaOH, $CO_2$, $H_2O$, TiO, Na, $H_2S$, CO, CrH, MgH, K, $PH_3$, NaOH, SiO, NaH, $CH_4$, $NH_3$, SiS |
| *Eq.* Profiles | 67 | 1500 | $CO_2$, TiO, $H_2O$, Na, CO, $H_2S$, MgH, CrH, K, SiO, $PH_3$, NaOH, AlO, PS, NaH, PO, $NH_3$, $CH_4$, SiS, $SiO_2$, SH |

**Note.**
[a] VMR of the species used in the transit depth simulation. [△]Volume metallicity in solar abundances.

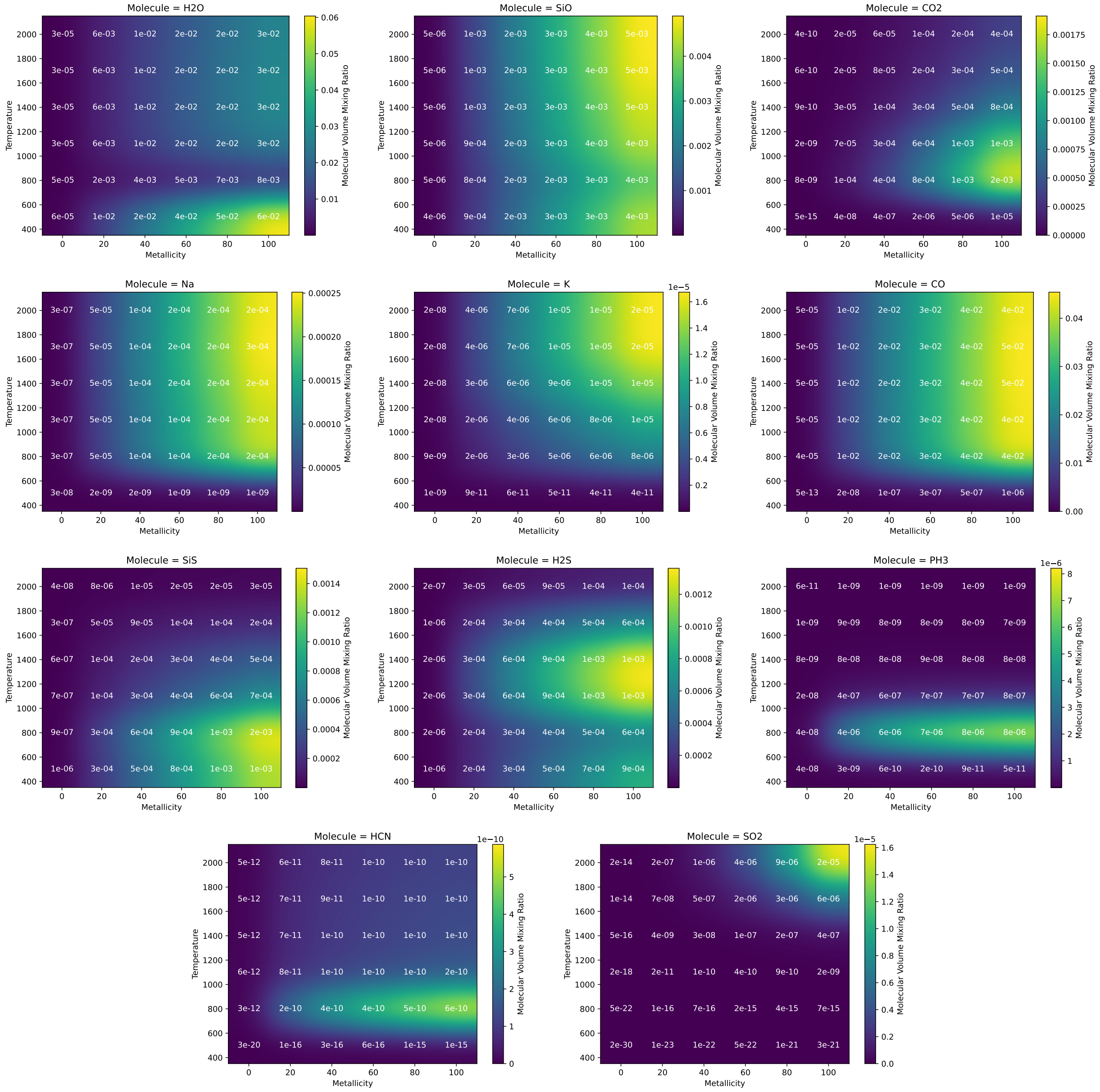

**Figure 19.** Examples of molecular abundances from equilibrium chemistry in the temperatures and metallicities regime of WASP-39 b's atmosphere. These plots showcase results at a pressure of ∼$10^{-3}$ bar. Note that the color scales vary for each plot.

## Appendix B
## Assessment of Retrieval Convergence

In both solutions reported in Section 3.2, $H_2O$ and $CO_2$ fit the main spectral features, while SiO supports the feature around 4.1 $\mu$m. Na and K align with features around 0.6 and 0.8 $\mu$m in the optical. Gray clouds provided the continuum from optical to near-infrared. In both cases, the HPS clouds contributed to the optical continuum. We show the details of the altitude-dependent optical depths and cloud contribution for the two solutions in Figure 20.

The maximum a posteriori (MAP) results, representing the statistical local optimization, are consistent with the medium values shown in Figure 4 above each histogram. The MAP values are the sets of parameter values that have the maximum likelihood. In well-constrained retrievals with chi-square posterior distributions, the set of median values is expected to fit the spectrum despite not being from the same retrieval sampling trace, which shows the good convergence of the algorithm. When the parameters follow a nonnormal probability distribution, the median values will not necessarily fit the spectrum; however, this should not be the case in our study, given the nature of the parameters we are investigating. We list the median values of posteriors and the first ten MAP traces in Table 4 of the two retrieval solutions of our reference model in Section 3.2.

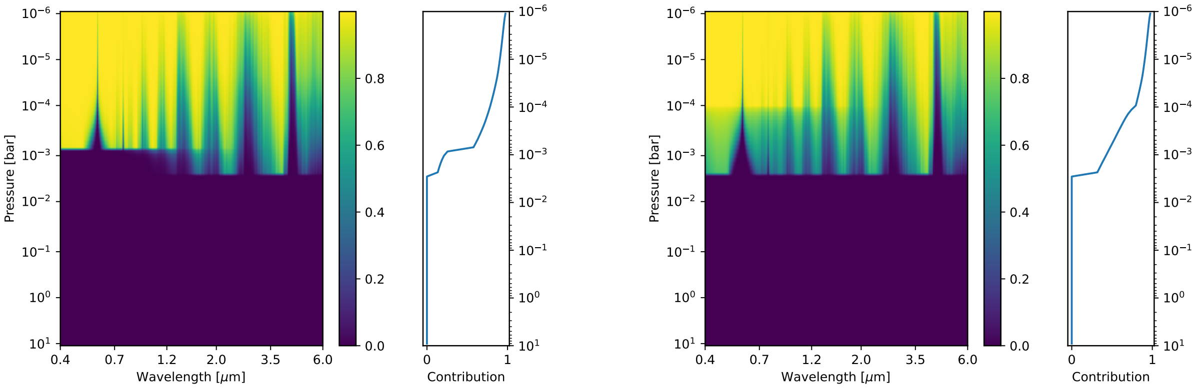

**Figure 20.** Optical depths for the two solutions identified by Step 2 free retrievals in Figure 4.

**Table 4**

Reference Model Retrieved Median and MAP Values of Two Solutions

| Value | $R_p$ ($R_J$) | $T$ (K) | log $\chi_{H_2O}$ | log $\chi_{CO_2}$ | log $\chi_{SiO}$ | log $\chi_{Na}$ | log $\chi_K$ | log $p_{gray}$ (Pa) | log $r_{HPS}$ (m) | log $N_{HPS}$ ($m^{-3}$) | log $p_{HPS, deck}$ (Pa) | log $p_{HPS, base}$ (Pa) | $\mu$ (Dalton) | Weight |
|---|---|---|---|---|---|---|---|---|---|---|---|---|---|---|
| NIRISS + NIRSpec + NIRCam Solution 1 | | | | | | | | | | | | | | |
| Median | 1.209 | 7.782e+02 | −1.629 | −3.118 | −1.818 | −3.024 | −5.434 | 2.406 | −6.755 | 6.906 | 1.921 | 3.142 | 3.377 | ⋯ |
| MAP 1 | 1.209 | 8.014e+02 | −1.704 | −3.221 | −1.721 | −3.035 | −5.247 | 2.424 | −6.655 | 6.738 | 1.930 | 2.967 | 3.461 | 7.277e-04 |
| MAP 2 | 1.209 | 7.898e+02 | −1.657 | −3.195 | −1.762 | −3.055 | −5.332 | 2.399 | −6.697 | 6.851 | 1.956 | 2.181 | 3.426 | 7.201e-04 |
| MAP 3 | 1.209 | 7.960e+02 | −1.695 | −3.169 | −1.714 | −3.013 | −5.232 | 2.456 | −6.839 | 7.119 | 1.914 | 2.168 | 3.486 | 6.555e-04 |
| MAP 4 | 1.209 | 7.877e+02 | −1.668 | −3.180 | −1.757 | −3.045 | −5.364 | 2.442 | −6.695 | 6.908 | 1.931 | 2.190 | 3.428 | 5.709e-04 |
| MAP 5 | 1.208 | 8.032e+02 | −1.714 | −3.259 | −1.728 | −3.070 | −5.499 | 2.456 | −6.835 | 7.103 | 1.955 | 3.099 | 3.439 | 5.512e-04 |
| MAP 6 | 1.211 | 7.930e+02 | −1.696 | −3.205 | −1.698 | −3.110 | −5.421 | 2.523 | −6.760 | 7.000 | 2.015 | 2.290 | 3.509 | 4.822e-04 |
| MAP 7 | 1.211 | 7.664e+02 | −1.711 | −3.205 | −1.776 | −3.217 | −5.562 | 2.460 | −6.749 | 6.953 | 2.017 | 2.294 | 3.357 | 4.751e-04 |
| MAP 8 | 1.210 | 7.952e+02 | −1.662 | −3.105 | −1.716 | −3.039 | −5.674 | 2.439 | −6.682 | 6.825 | 1.919 | 2.182 | 3.510 | 4.524e-04 |
| MAP 9 | 1.211 | 7.635e+02 | −1.728 | −3.194 | −1.771 | −3.204 | −5.478 | 2.541 | −6.782 | 6.947 | 2.043 | 3.858 | 3.355 | 4.513e-04 |
| MAP 10 | 1.208 | 7.939e+02 | −1.735 | −3.244 | −1.745 | −3.108 | −5.507 | 2.444 | −6.716 | 6.853 | 1.972 | 3.140 | 3.394 | 4.472e-04 |
| NIRISS + NIRSpec + NIRCam Solution 2 | | | | | | | | | | | | | | |
| Median | 1.208 | 7.640e+02 | −1.687 | −3.157 | −1.857 | −3.239 | −5.942 | 2.403 | −6.290 | 3.817 | 1.156 | 2.792 | 3.264 | ⋯ |
| MAP 1 | 1.209 | 7.875e+02 | −1.736 | −3.163 | −1.739 | −3.257 | −5.788 | 2.395 | −6.263 | 3.686 | 1.099 | 3.987 | 3.403 | 1.136e-03 |
| MAP 2 | 1.208 | 7.769e+02 | −1.749 | −3.201 | −1.783 | −3.322 | −5.740 | 2.443 | −6.192 | 3.499 | 1.006 | 3.514 | 3.318 | 1.134e-03 |
| MAP 3 | 1.210 | 7.687e+02 | −1.720 | −3.163 | −1.754 | −3.347 | −6.174 | 2.540 | −6.257 | 3.676 | 1.030 | 3.619 | 3.386 | 9.423e-04 |
| MAP 4 | 1.208 | 7.806e+02 | −1.780 | −3.249 | −1.784 | −3.354 | −5.972 | 2.400 | −6.320 | 3.781 | 1.077 | 3.560 | 3.293 | 9.354e-04 |
| MAP 5 | 1.208 | 7.759e+02 | −1.740 | −3.235 | −1.789 | −3.352 | −5.993 | 2.449 | −6.372 | 3.888 | 1.037 | 3.369 | 3.311 | 9.112e-04 |
| MAP 6 | 1.209 | 7.846e+02 | −1.740 | −3.204 | −1.740 | −3.215 | −5.996 | 2.420 | −6.362 | 3.849 | 1.039 | 3.581 | 3.398 | 8.759e-04 |
| MAP 7 | 1.211 | 7.801e+02 | −1.728 | −3.195 | −1.717 | −3.346 | −5.764 | 2.517 | −6.221 | 3.577 | 1.082 | 3.235 | 3.443 | 8.450e-04 |
| MAP 8 | 1.207 | 7.845e+02 | −1.671 | −3.167 | −1.819 | −3.242 | −5.786 | 2.361 | −6.382 | 3.990 | 1.010 | 1.770 | 3.321 | 7.704e-04 |
| MAP 9 | 1.209 | 7.867e+02 | −1.748 | −3.202 | −1.734 | −3.232 | −5.628 | 2.370 | −6.401 | 3.943 | 1.038 | 3.813 | 3.403 | 7.475e-04 |
| MAP 10 | 1.210 | 7.750e+02 | −1.700 | −3.152 | −1.754 | −3.306 | −5.856 | 2.529 | −6.249 | 3.636 | 1.101 | 3.388 | 3.401 | 6.851e-04 |

## Appendix C
## Testing Retrieval Degeneracy: Atmospheric Scale Height

After optimizing the retrieval simulations in Step 2 using a minimal set of free parameters (reference model), we introduced higher retrieval freedom by allowing the algorithm to adjust the scale height through the mean molecular weight. By incorporating $N_2$ and Li as representative gases for heavy and light spectrally inactive species, this approach avoids

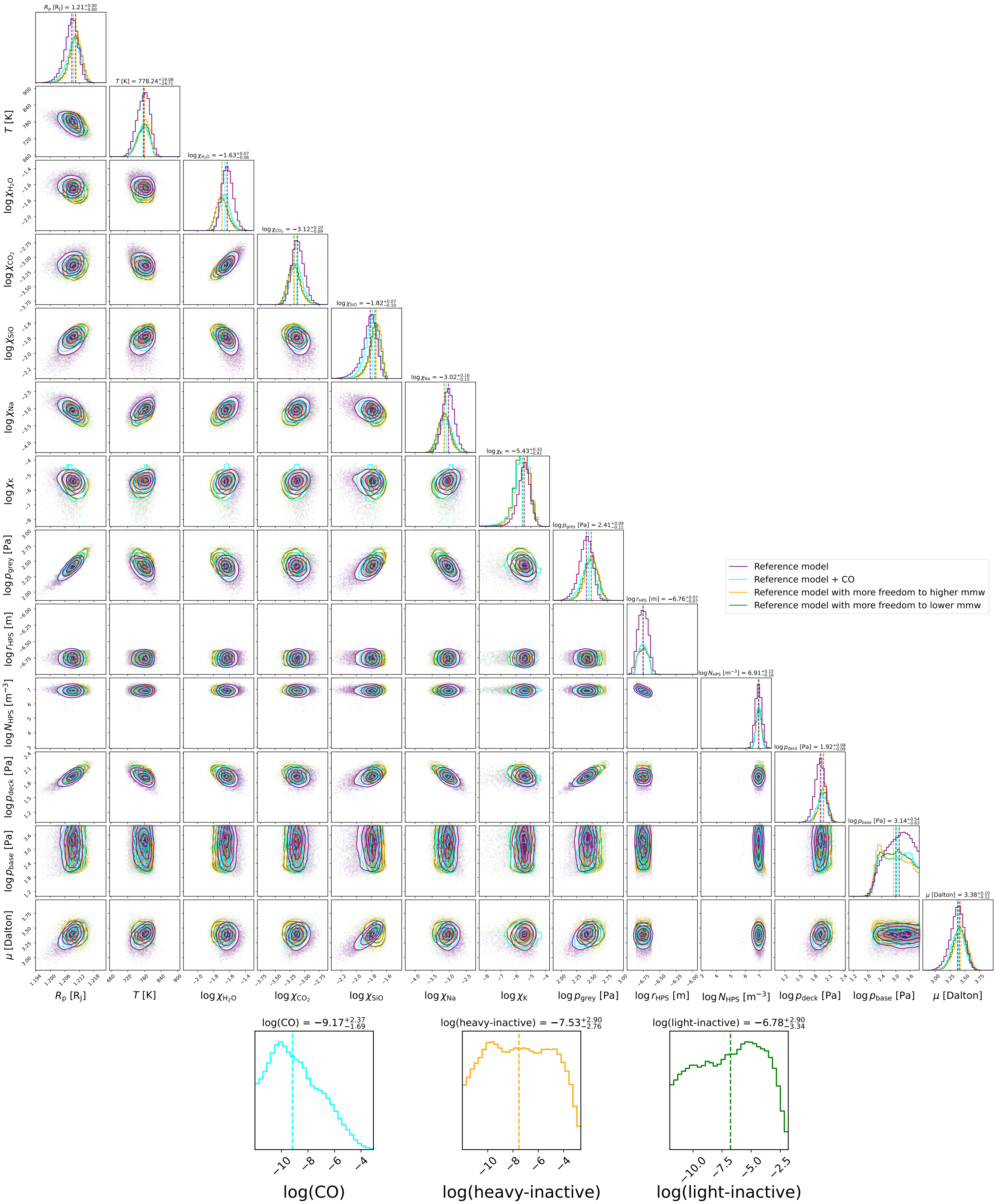

**Figure 21.** Posterior comparison (Solution 1) of retrievals of the reference model in Step 2 (purple), with CO (cyan), with $N_2$ to have more freedom to higher mean molecular weight (yellow), and with Li to have more freedom to lower mean molecular weight (green).

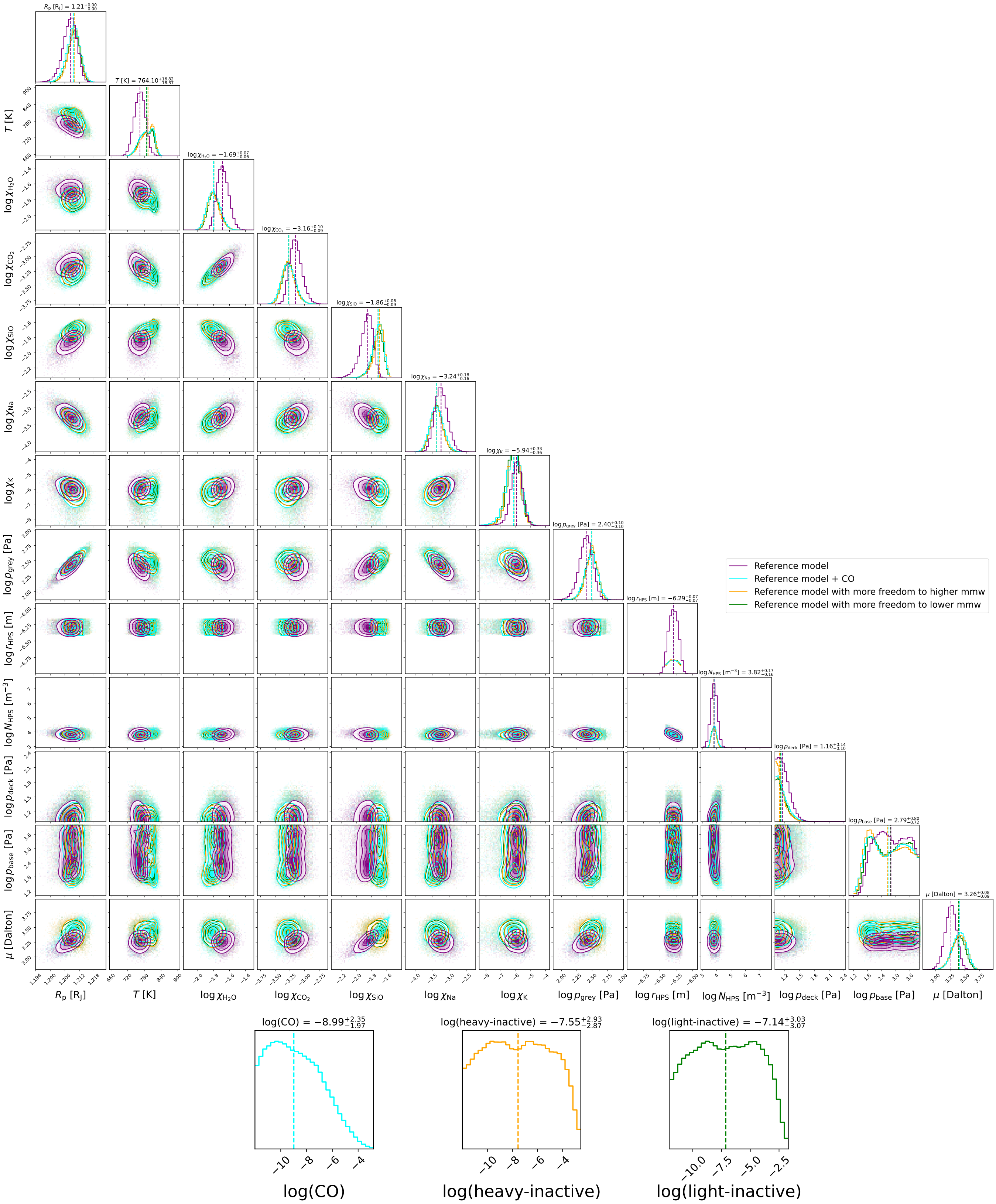

**Figure 22.** Posterior comparison (Solution 2) of the four models in Figure 21.

introducing unwanted spectral signatures from the added species. Additionally, we include CO, which was excluded from the reference model in Step 2, to decrease the retrieval dimensionality due to its features largely being masked by $H_2O$ and $CO_2$, although it has been suggested in molecular selection alongside other molecules in Step 1.

We present the posterior distributions in Figures 21 (Solution 1) and 22 (Solution 2). The results from the other three models show no significant deviation from the reference model in either solution. None of the models constrains the abundances of CO, $N_2$, or Li.

## ORCID iDs

Sushuang Ma https://orcid.org/0000-0001-9010-0539
Arianna Saba https://orcid.org/0000-0002-1437-4228
Ahmed Faris Al-Refaie https://orcid.org/0000-0003-2241-5330
Giovanna Tinetti https://orcid.org/0000-0001-6058-6654
Sergei N. Yurchenko https://orcid.org/0000-0001-9286-9501
Jonathan Tennyson https://orcid.org/0000-0002-4994-5238
Cesare Cecchi-Pestellini https://orcid.org/0000-0001-7480-0324

## References

Ackerman, A. S., & Marley, M. S. 2001, ApJ, 556, 872
Agúndez, M., Martínez, J. I., de Andres, P. L., Cernicharo, J., & Martín-Gago, J. A. 2020, A&A, 637, A59
Agúndez, M., Venot, O., Iro, N., et al. 2012, A&A, 548, A73
Ahrer, E.-M., Stevenson, K. B., Mansfield, M., et al. 2023, Natur, 614, 653
Al-Refaie, A. F., Changeat, Q., Venot, O., Waldmann, I. P., & Tinetti, G. 2022, ApJ, 932, 123
Al-Refaie, A. F., Changeat, Q., Waldmann, I. P., & Tinetti, G. 2021, ApJ, 917, 37
Alderson, L., Grant, D., & Wakeford, H. 2022, Exo-TiC/ExoTiC-JEDI: v0.1-beta-release Zenodo, doi: 10.5281/zenodo.7185855
Alderson, L., Wakeford, H. R., Alam, M. K., et al. 2023, Natur, 614, 664
Allard, N. F., Spiegelman, F., & Kielkopf, J. F. 2016, A&A, 589, A21
Allard, N. F., Spiegelman, F., Leininger, T., & Molliere, P. 2019, A&A, 628, A120
Arfaux, A., & Lavvas, P. 2024, MNRAS, 530, 482
Asplund, M., Grevesse, N., Sauval, A. J., & Scott, P. 2009, ARA&A, 47, 481
Astropy Collaboration, Price-Whelan, A. M., Lim, P. L., et al. 2022, ApJ, 935, 167
Astropy Collaboration, Price-Whelan, A. M., Sipőcz, B. M., et al. 2018, AJ, 156, 123
Astropy Collaboration, Robitaille, T. P., Tollerud, E. J., et al. 2013, A&A, 558, A33
Azzam, A. A. A., Tennyson, J., Yurchenko, S. N., & Naumenko, O. V. 2016, MNRAS, 460, 4063
Bell, T., Ahrer, E.-M., Brande, J., et al. 2022, JOSS, 7, 4503
Benneke, B., Wong, I., Piaulet, C., et al. 2019, ApJL, 887, L14
Bohren, C. F., & Huffman, D. R. 2008, Absorption and Scattering of Light by Small Particles (Wiley)
Bonomo, A. S., Desidera, S., Benatti, S., et al. 2017, A&A, 602, A107
Bourrier, V., Kitzmann, D., Kuntzer, T., et al. 2020, A&A, 637, A36
Buchner, J., Georgakakis, A., Nandra, K., et al. 2014, A&A, 564, A125
Carter, A. L., May, E. M., Espinoza, N., et al. 2024, NatAs, 8, 1008
Changeat, Q., Bardet, D., Chubb, K., et al. 2025, A&A, 699, A219
Changeat, Q., Edwards, B., Al-Refaie, A. F., et al. 2022, ApJS, 260, 3
Changeat, Q., Ito, Y., Al-Refaie, A. F., Yip, K. H., & Lueftinger, T. 2024, AJ, 167, 195
Chen, Z., Ji, J., Chen, G., Yan, F., & Tan, X. 2025, AJ, 169, 294
Chubb, K. L., Robert, S., Sousa-Silva, C., et al. 2024, RASTI , 3, 636
Chubb, K. L., Rocchetto, M., Yurchenko, S. N., et al. 2021, A&A, 646, A21
Coles, P. A., Yurchenko, S. N., & Tennyson, J. 2019, MNRAS, 490, 4638
Constantinou, S., & Madhusudhan, N. 2024, MNRAS, 530, 3252
Cox, A. N. 2015, Allen's Astrophysical Quantities (4th ed.; Springer)
Darveau-Bernier, A., Albert, L., Talens, G. J., et al. 2022, PASP, 134, 094502
Davey, J. J., Yip, K. H., Al-Refaie, A. F., & Waldmann, I. P. 2024, MNRAS, 536, 2618
Deirmendjian, D. 1964, ApOpt, 3, 187
Dorschner, J., Begemann, B., Henning, T., Jaeger, C., & Mutschke, H. 1995, A&A, 300, 503
Esparza-Borges, E., López-Morales, M., Adams Redai, J. I., et al. 2023, ApJL, 955, L19
Espinoza, N. 2022, TransitSpectroscopy, v0.3.11 Zenodo, doi:10.5281/zenodo.6960924
Espinoza, N., Kossakowski, D., & Brahm, R. 2019, MNRAS, 490, 2262
Fabian, D., Jäger, C., Henning, T., Dorschner, J., & Mutschke, H. 2000, A&A, 364, 282
Faedi, F., Barros, S. C. C., Anderson, D. R., et al. 2011, A&A, 531, A40
Feinstein, A. D., Radica, M., Welbanks, L., et al. 2023, Natur, 614, 670
Feroz, F., & Hobson, M. P. 2008, MNRAS, 384, 449
Feroz, F., Hobson, M. P., & Bridges, M. 2009, MNRAS, 398, 1601
Feroz, F., Hobson, M. P., Cameron, E., & Pettitt, A. N. 2019, OJAp, 2, 10
Fischer, P. D., Knutson, H. A., Sing, D. K., et al. 2016, ApJ, 827, 19
Fisher, C., & Heng, K. 2018, MNRAS, 481, 4698
Fisher, C., Taylor, J., Parmentier, V., et al. 2024, MNRAS, 535, 27
Flagg, L., Weinberger, A. J., Bell, T. J., et al. 2024, ApJ, 969, L19
Gierasch, P., & Conrath, B. 1985, Recent Advances in Planetary Meteorology (G. E. Hunt; Cambridge: Cambridge Univ. Press), 121
Gorman, M. N., Yurchenko, S. N., & Tennyson, J. 2019, MNRAS, 490, 1652
Grant, D., Lothringer, J. D., Wakeford, H. R., et al. 2023, ApJL, 949, L15
Harris, C. R., Millman, K. J., van der Walt, S. J., et al. 2020, Natur, 585, 357
Hinkel, N. R., Young, P. A., & Wheeler, C. H. I. 2022, AJ, 164, 256
Holmberg, M., & Madhusudhan, N. 2023, MNRAS, 524, 377
Jaeger, C., Molster, F. J., Dorschner, J., et al. 1998, A&A, 339, 904
Jaeger, C., Mutschke, H., Begemann, B., Dorschner, J., & Henning, T. 1994, A&A, 292, 641
Jäger, C., Dorschner, J., Mutschke, H., Posch, T., & Henning, T. 2003, A&A, 408, 193
JWST Transiting Exoplanet Community Early Release Science Team, Ahrer, E.-M., Alderson, L., et al. 2023, Natur, 614, 649
Karman, T., Gordon, I. E., van der Avoird, A., et al. 2019, Icar, 328, 160
Kempton, E. M. R., Zhang, M., Bean, J. L., et al. 2023, Natur, 620, 67
Khorshid, N., Min, M., Polman, J., & Waters, L. B. F. M. 2024, A&A, 685, A64
Kirk, J., López-Morales, M., Wheatley, P. J., et al. 2019, AJ, 158, 144
Kitzmann, D., Heng, K., Oreshenko, M., et al. 2020, ApJ, 890, 174
Lam, S. K., Pitrou, A., & Seibert, S. 2015, in Proc. Second Workshop on the LLVM Compiler Infrastructure in HPC, 1
Lendl, M., Cubillos, P. E., Hagelberg, J., et al. 2017, A&A, 606, A18
Lendl, M., Delrez, L., Gillon, M., et al. 2016, A&A, 587, A67
Lodders, K. 2021, SSRv, 217, 44
Louca, A. J., Miguel, Y., & Kubyshkina, D. 2023, ApJL, 956, L19
Lueber, A., Novais, A., Fisher, C., & Heng, K. 2024, A&A, 687, A110
Ma, S., Ito, Y., Al-Refaie, A. F., et al. 2023, ApJ, 957, 104
Maciejewski, G., Dimitrov, D., Mancini, L., et al. 2016, AcA, 66, 55
Mancini, L., Esposito, M., Covino, E., et al. 2018, A&A, 613, A41
McKemmish, L. K., Masseron, T., Hoeijmakers, H. J., et al. 2019, MNRAS, 488, 2836
McKemmish, L. K., Yurchenko, S. N., & Tennyson, J. 2016, MNRAS, 463, 771
Mugnai, L. V., Swain, M. R., Estrela, R., & Roudier, G. M. 2024, MNRAS, 531, 35
Nikolov, N., Sing, D. K., Gibson, N. P., et al. 2016, ApJ, 832, 191
Niraula, P., de Wit, J., Gordon, I. E., Hargreaves, R. J., & Sousa-Silva, C. 2023, ApJL, 950, L17
Novais, A., Fisher, C., Ghezzi, L., et al. 2025, MNRAS, 538, 2521
Owens, A., Tennyson, J., & Yurchenko, S. N. 2021, MNRAS, 502, 1128
Pinhas, A., Madhusudhan, N., Gandhi, S., & MacDonald, R. 2019, MNRAS, 482, 1485
Pinhas, A., Rackham, B. V., Madhusudhan, N., & Apai, D. 2018, MNRAS, 480, 5314
Polanski, A. S., Crossfield, I. J. M., Howard, A. W., Isaacson, H., & Rice, M. 2022, RNAAS, 6, 155
Polyansky, O. L., Kyuberis, A. A., Zobov, N. F., et al. 2018, MNRAS, 480, 2597
Powell, D., Feinstein, A. D., Lee, E. K. H., et al. 2024, Natur, 626, 979
Prajapat, L., Jagoda, P., Lodi, L., et al. 2017, MNRAS, 472, 3648
Radica, M. 2024, JOSS, 9, 6898
Radica, M., Welbanks, L., Espinoza, N., et al. 2023, MNRAS, 524, 835
Rigby, J., Perrin, M., McElwain, M., et al. 2023, PASP, 135, 048001
Rivlin, T., Lodi, L., Yurchenko, S. N., Tennyson, J., & Le Roy, R. J. 2015, MNRAS, 451, 634
Rocchetto, M., Waldmann, I. P., Venot, O., Lagage, P. O., & Tinetti, G. 2016, ApJ, 833, 120
Roy-Perez, J., Pérez-Hoyos, S., Barrado-Izagirre, N., Chen-Chen, H., et al. 2025, A&A, 694, A249
Rustamkulov, Z., Sing, D. K., Liu, R., & Wang, A. 2022, ApJL, 928, L7

Rustamkulov, Z., Sing, D. K., Mukherjee, S., et al. 2023, Natur, 614, 659
Saba, A., Thompson, A., Hou Yip, K., et al. 2025, ApJS, 276, 70
Sarkar, S., Madhusudhan, N., Constantinou, S., & Holmberg, M. 2024, MNRAS, 531, 2731
Schleich, S., Boro Saikia, S., Changeat, Q., et al. 2024, A&A, 690, A336
Scott, A., & Duley, W. W. 1996, ApJS, 105, 401
Semenov, M., El-Kork, N., Yurchenko, S. N., & Tennyson, J. 2025, MNRAS, 536, 714
Sing, D. K., Fortney, J. J., Nikolov, N., et al. 2016, Natur, 529, 59
Skinner, J. W., & Wei, S. 2025, ApJ, 995, 9
Sousa-Silva, C., Hesketh, N., Yurchenko, S. N., Hill, C., & Tennyson, J. 2014, JQSRT, 142, 66
Stock, J. W., Kitzmann, D., Patzer, A. B. C., & Sedlmayr, E. 2018, MNRAS, 479, 865
Swain, M. R., Hasegawa, Y., Thorngren, D. P., & Roudier, G. M. 2024, SSRv, 220, 61
Tada, S., Kawahara, H., Kawashima, Y., Kotani, T., & Masuda, K. 2025, AJ, 169, 255
Tennyson, J., Yurchenko, S. N., Zhang, J., et al. 2024, JQSRT, 326, 109083
Thompson, A., Biagini, A., Cracchiolo, G., et al. 2024, ApJ, 960, 107
Thorngren, D., & Fortney, J. J. 2019, ApJL, 874, L31
Tsai, S.-M., Lee, E. K. H., Powell, D., et al. 2023a, Natur, 617, 483
Tsai, S.-M., Moses, J. I., Powell, D., & Lee, E. K. H. 2023b, ApJL, 959, L30
Tsiaras, A., Waldmann, I. P., Rocchetto, M., et al. 2016, ApJ, 832, 202
Tsiaras, A., Waldmann, I. P., Zingales, T., et al. 2018, AJ, 155, 156
Underwood, D. S., Tennyson, J., Yurchenko, S. N., et al. 2016, MNRAS, 459, 3890
Upadhyay, A., Conway, E. K., Tennyson, J., & Yurchenko, S. N. 2018, MNRAS, 477, 1520
Veillet, R., Venot, O., Sirjean, B., et al. 2026, A&A, 706, A260
Virtanen, P., Gommers, R., Oliphant, T. E., et al. 2020, NatMe, 17, 261
Visscher, C., Lodders, K., & Fegley, B., Jr. 2010, ApJ, 716, 1060
Wakeford, H. R., Sing, D. K., Deming, D., et al. 2018, AJ, 155, 29
Woitke, P., Helling, C., Hunter, G. H., et al. 2018, A&A, 614, A1
Yip, K. H., Changeat, Q., Edwards, B., et al. 2021, AJ, 161, 4
Yurchenko, S. N., Mellor, T. M., Freedman, R. S., & Tennyson, J. 2020, MNRAS, 496, 5282
Yurchenko, S. N., Owens, A., Kefala, K., & Tennyson, J. 2024, MNRAS, 528, 3719
Yurchenko, S. N., Tennyson, J., Syme, A.-M., et al. 2022, MNRAS, 510, 903
Zeidler, S., Mutschke, H., & Posch, T. 2015, ApJ, 798, 125
Zeidler, S., Posch, T., & Mutschke, H. 2013, A&A, 553, A81